Instability-driven Magnetohydrodynamic Turbulence

by

Justin W. Walker

A dissertation submitted in partial fulfillment of
the requirements for the degree of

Doctor of Philosophy

(Physics)

at the

UNIVERSITY OF WISCONSIN–MADISON

2019

Date of final oral examination: November 1, 2019

The dissertation is approved by the following members of the Final Oral Committee:

Stanislav Boldyrev, Professor, Physics
Cary Forest, Professor, Physics
Paul Terry, Professor, Physics
Ellen Zweibel, Professor, Astronomy and Physics

To my parents, Doreen and Kenneth.

ACKNOWLEDGMENTS

There are many people without whose help I would not have made it to this point. First, I would like to thank my advisor Stas Boldyrev for giving me his confidence and support throughout graduate school, for guiding me toward interesting research projects, for being generous with his time and expertise, and for being incredibly accommodating to my geographic wandering.

Many thanks to Geoffroy Lesur for introducing me to the field of accretion disk dynamics, for many fruitful discussions, and, of course, for writing SNOOPY. I thank Nuno Loureiro for a productive collaboration and for his sharp ideas. I also thank Vladimir Zhdankin for camaraderie and for pointing me toward some interesting research.

There are several people I need to thank who were key to my even finding my way into graduate school. Thank you to Cary Forest for giving a colloquium at the University of Chicago that really sparked my interest in plasmas, MHD, and the dynamo. I would like to thank Bob Rosner for guiding a clueless, but enthusiastic, undergraduate to capitalize on that interest. Many thanks to Fausto Cattaneo for mentoring and for insightful discussions over the last ten years. I can never thank enough Andrew Siegel who gave me a chance to prove myself. Thank you to those at Argonne with whom I had the privilege of working and learning: Paul Fischer, Aleks Obabko, Elia Merzari, Shashi Aithal, Katy Heisey, and Yulia Peet.

My time in Madison would not have been as memorable and rich without the friends—new and old—who helped me maintain a sense of balance. A special thanks to the Cascave: Adrian, Ben, Garth, Zach, Ian, and Jason. In addition to useful discussions of research, you all provided very needed affirmation and diversion, as well as sunshine to an otherwise intermittently dark, or fluorescent, or dark, space. Mitch, my brother, I was uplifted every time I watched, from blocks away, your towering frame, with beard and

Carhart, amble towards me for our rendezvous. Lila and Daniel, thank you for your warm hearts and open home, where I found frequent respite—and dinner—in times of stress. Thank you Victor for eclectic conversation, for inviting me to sit, even virtually, at the table on Wednesday nights, and for numerous car rides around Madison. The shore and waters of Lake Mendota proved to be grounding and calming. To the sailing crew at Hoofers, I owe an enormous thank you for creating a communal atmosphere: Yun, Olivier, Joel, Pedro, Barry, Andy, and last but *certainly* not least, Pete. Ekmel, you were a truly great roommate for our five years together; what a rarity that a friendship was grown, rather than strained, out of such an experience. To Emily, Vanessa, Obi, and John, thank you for the far-ranging discussions and support.

To my friends in Chicago—Carmen, Greg, Hannah, Michael, and Irmak—thank you for making me feel at home during my frequent visits.

I want to thank those lifelong friends whose support was felt, even in absentia: Anthony, Brad, Dave, Daniel, Eric, Kyle, Luis, and Szilard.

This all started with an assignment from my high school English teacher and the guidance from my physics teacher. I thank Mr. and Mrs. Oser for inspiring me to reach high and to pursue life as a scientist.

To Bo, when things were difficult for me, you stood by my side and gave me the encouragement I needed. You sacrificed so that I could achieve my goals. Thank you.

Finally, I thank my family. I could not have done this without your love and support.

CONTENTS

LIST OF TABLES

LIST OF FIGURES

ABSTRACT

Instability-driven turbulence is ubiquitous in astrophysical and laboratory plasmas, where it is an important component to how these systems transport energy, momentum, particles, etc. This thesis is concerned with how two instabilities drive and interact with magnetohydrodynamic turbulence.

The magnetorotational instability (MRI) is the best candidate for driving turbulence in well-ionized accretion disks. In this thesis, the turbulence driven by the MRI is studied with a particular focus on how it compares to strong, driven, incompressible MHD turbulence. High-resolution, high-Reynolds number setups are analyzed to determine the existence and character of an inertial range of scales where a nonlinear cascade dominates the dynamics.

In contrast to previous studies, systems with an imposed magnetic field—that activate the linear MRI—provide evidence for the existence of an inertial range when one considers the dynamics perpendicular to a strong, large-scale axial magnetic field that develops in the system. The outer scale of the turbulence is determined by balance between the linear shear, present at all scales, and the turbulent shear.

In the case of a system without an imposed magnetic field—where the MRI dynamo is subcritical—evidence is found for self-sustained turbulence at magnetic Prandtl number $\mathrm{Pm} = 1$. Previous work was not able produce such turbulence for systems at lower Reynolds numbers. A turbulent state is found to be easier to self-sustain in these systems in high-aspect-ratio domains, with angular momentum transport also highly dependent on aspect ratio. Vertically-extended domains exhibit higher transport. Azimuthally-extended domains show increased transport until a certain aspect ratio, beyond which the transport decreases. A phenomenological explanation is proposed by which the separation of toroidal magnetic flux vertically allows for increased transport and drive of the subcritical MRI dynamo; as the

toroidal dimension is extended, the tearing mode acts to break up such large scale flux, reducing transport.

Additionally, two-dimensional MHD turbulence is studied in order to test the predictions of new theories that hypothesize competition between the tearing mode and turbulent fluctuations in flows with high Lundquist number. A method is introduced to simulate evolution of single, critically-balanced eddy, thereby allowing the direct investigation of this competition. Results demonstrate the disruption of the correlated eddy structure on the shorter of the Alfvén or tearing time. Steepening of the energy spectrum is observed, while decreased alignment is not. Generally, these results support the proposed theory, with further investigation warranted.

1 INTRODUCTION

Astrophysical systems are characterized by their enormous size, which has two important consequences. First, when compared to systems of smaller size, the role played by gravity changes from being minor to major, even central, to describing the problem. Second, the size can lead to a separation of scales of many orders of magnitude between the microphysical scales associated with individual particle interactions and the linear dimension of the whole system. Because of the first of these, objects such as stars or astrophysical disks have large reservoirs of gravitational potential energy that can be converted into other forms of energy—kinetic, magnetic, heat—through some mechanism. That mechanism often comes in the form of some instability.

In general, when an equilibrium configuration can easily rearrange itself to release free energy, an instability will tend to drive the system away from that equilibrium, toward another. For example, the Rayleigh-Taylor instability occurs when a heavier fluid is balanced on top of a lighter fluid. Naturally, the system is at a lower potential energy state when the heavier fluid is on bottom and, thus, a disturbance from equilibrium will drive it in this direction.

Because of the large scale-separation in natural plasma systems, such as the interstellar medium, the solar corona, solar wind, accretion disks, etc., instabilities can drive turbulence that spans a very broad range of scales (e.g., Biskamp, 2003). This affects important phenomena like plasma heating, particle acceleration and scattering (e.g., Chen, 2016), as well as the affecting the fundamental dynamics of a system, such as in accretion disks (Shakura and Sunyaev, 1973).

At scales larger than the ion kinetic scales, the plasma dynamics can be modeled in the framework of magnetohydrodynamics (MHD) (e.g., Biskamp, 2003; Chen, 2016; Tobias et al., 2013; Davidson, 2017; Chen and Boldyrev,

2017). In MHD, the nonlinear interaction of fluid eddies results in the transfer of energy from the driving scale to the dissipation scales through a scale-by-scale "cascade."[1] Because instabilities are frequently present at large scales to drive flows in astrophysical systems, there exists a richness of phenomena in astrophysics described by instability-driven turbulence, whose ultimate source is gravitational energy.

In this thesis, we study magnetohydrodynamic turbulence driven by and competing with local instabilities. First, we will study the local turbulence in accretion disks driven by the magnetorotational instability (MRI) by using the "shearing-box," or "shearing-sheet," equations (Goldreich and Lynden-Bell, 1965; Hawley et al., 1995; Umurhan and Regev, 2004). Second, we will investigate the effects of the tearing instability on MHD turbulence, motivated by recent theoretical models of "tearing-mediated turbulence." The primary method of investigation will be the analysis of large-scale computations of fully nonlinear solutions to the MHD equations.

The remainder of this chapter will provide background and motivational material for the work contained in subsequent chapters. Section 1.1 will review thin accretion turbulence. Section 1.2 will describe the linear magnetorotational instability. Section 1.3 will discuss magnetohydrodynamics and turbulence phenomenology, including the new tearing-mediated regime. Section 1.4 will describe the shearing box model used in this thesis. Section 1.5 will describe the numerical methods used.

1.1 Turbulence in accretion disks

Black holes, compact objects from which even light cannot escape, are observable electromagnetically from their interaction with the matter that surrounds them (Event Horizon Telescope Collaboration et al., 2019). This

[1] This is best understood in the fluid context, but generalizations do exist (e.g., Schekochihin et al., 2009).

matter will accrete onto the black hole forming a disk—unless there is no rotation in the system, a situation known as Bondi accretion—the precise shape of which depends on relative strengths of gravity, pressure, and rotation (e.g., Abramowicz and Fragile, 2013). In the process of falling toward the event horizon, matter can be heated or even ejected in the form of jets. Radiation from the accelerated and heated gas in the disk is emitted over a broad range of the electromagnetic spectrum and can be observed from these very luminous objects, e.g. active galactic nuclei (AGN). As the best candidate for driving the turbulence and angular momentum transport responsible for accretion onto black holes, the MRI is an essential component in what is one of the most energetic, efficient energy-conversion processes in the universe (e.g., Abramowicz and Fragile, 2013).

Based on work by (Shakura and Sunyaev, 1973), black holes were predicted to be strongly luminous objects of X-ray radiation due to the heating of gas in the hot, central regions of a thin, rotating disk around the black hole. The luminosity is directly connected to the matter inflow rate of mass accreting onto a disk around the black hole. Because the gas comprising the disk is in Keplerian or near-Keplerian orbit with an effective potential due to its angular momentum, this rate of accretion is dependent on the outward flow of angular momentum. If one assumes diffusion of angular momentum due to fluid elements interacting through viscous stresses, then the accretion rate calculated is much smaller than what is observed, indicating the operation of some other mechanism. In Shakura and Sunyaev (1973), it was proposed that instead of a molecular viscosity, models should use a turbulent viscosity. Additionally, the exact process responsible need not be understood, and the efficiency of angular momentum transport could be parameterized by a dimensionless α. This transport parameter is proportional to Reynolds and Maxwell stresses within the disk.

Given the small viscosities of these disks, the corresponding Reynolds numbers are large (Spitzer, 1962), high enough that one would expect

the flow to be turbulent should there be some driving mechanism such as an instability. However, it can be shown that disks with Keplerian and nearly Keplerian profiles are hydrodynamically stable. Therefore, the turbulence must be driven by either a subcritical hydrodynamic instability or a magnetohydrodynamic instability.

Balbus and Hawley (1991) rediscovered a linear instability in magnetized, rotating fluids, critically connecting it to the evolution of accretion disks. Originally derived by Velikhov (1959) and Chandrasekhar (1960), what is known as the magnetorotational instability is active in differentially rotating plasmas or conducting fluids with a weak magnetic field. Besides accretion disks, it has been studied in the context of the solar dynamo (Kagan and Wheeler, 2014) and the geodynamo (Petitdemange et al., 2008). Additionally, the MRI is a prototype of subcritical magnetic dynamo action (Rincon et al., 2007; Herault et al., 2011; Riols et al., 2013).

Many analytic, numerical, and laboratory studies have been devoted to the onset of the instability and the resulting magnetic turbulence (e.g., Sisan et al., 2004; Gissinger et al., 2011; Seilmayer et al., 2014; Flanagan et al., 2015; Meheut et al., 2015; Latter et al., 2015). Systems exhibiting the MRI are dynamically complex, as they incorporate the effects of stratification, global geometry, boundary conditions, etc. Therefore, it is not currently possible to address the full-scale natural dynamics. While the MRI may be important for global angular momentum transport and accretion, it is a local, incompressible instability and can be studied by the use of local, reduced models. The shearing box is one such model that isolates the principal ingredients required for the MRI (e.g., Goldreich and Lynden-Bell, 1965; Hawley et al., 1995; Fromang et al., 2007; Longaretti and Lesur, 2010; Lesur and Longaretti, 2011; Riols et al., 2015). In the framework of the shearing box, the local and fundamental properties of MRI-driven turbulence may be studied. Modeling of the small-scale dynamics proves useful by producing values for the angular momentum transport coefficient α that can be used

in global modeling of the disk, star, or planet interior (e.g., Shakura and Sunyaev, 1973; Lesur and Ogilvie, 2010).

1.2 Magnetorotational instability

Consider a differentially rotating flow of an electrically conducting fluid or plasma that is threaded by a magnetic field. When nearby orbiting fluid elements connected by this magnetic field are displaced slightly, the magnetic field acts as a spring pulling them toward each other. For a strong field, magnetic tension will be strong enough to pull the fluid elements back together and they will circle each other at the epicyclic frequency $\kappa^2 = 2\Omega^2(2-q)$. For a weak field, the magnetic tension is not enough to restore the displacement and, instead, destabilizes the configuration by allowing the two elements to exchange angular momentum. This reduces the angular momentum of the inner element and increases that of the outer element, causing them to spiral further inward and outward, respectively. See the diagram in Figure 1.1.

If one considers a local, Cartesian coordinate system, rotating in a disk with radial coordinate x, azimuthal coordinate y, vertical coordinate z, and magnetic field $\boldsymbol{B} = B\hat{\boldsymbol{z}}$, then the MRI system can be described by the simple system of equations

$$\ddot{x} = \quad 2\Omega\dot{y} + 3\Omega^2 x - \omega_{\rm A}^2 x, \tag{1.1}$$

$$\ddot{y} = \underbrace{-2\Omega\dot{x}}_{\text{Coriolis}} \underbrace{\qquad}_{\text{tidal}} \underbrace{-\,\omega_{\rm A}^2 y}_{\text{spring}}, \tag{1.2}$$

where Ω is the disk rotation rate, and $\omega_{\rm A} \equiv k_\parallel v_{\rm A} = \boldsymbol{k} \cdot \frac{\boldsymbol{B}}{\sqrt{4\pi\varrho}}$ is the Alfvén frequency. One can see that in this equation the magnetic field acts as a spring or restoring force, while the Coriolis force exchanges momentum between components, and the tidal force accelerates the fluid element.

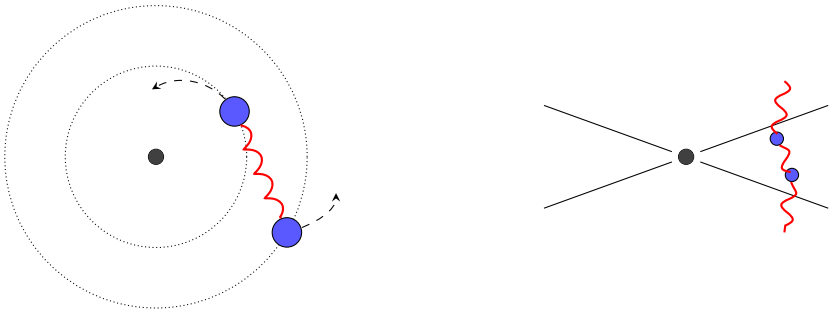

Figure 1.1: Cartoon diagram of MRI, showing the fluid elements in blue and the connecting magnetic field in red. On the left, the disk is seen from above, and the magnetic field, acting like a spring between the two fluid elements, causes the inner fluid element to move radially inward and the outer fluid element to move radially outward. On the right, the disk is seen from the side emphasizing that the most unstable mode of the instability—and most important when considering net vertical flux—is a small k_z mode.

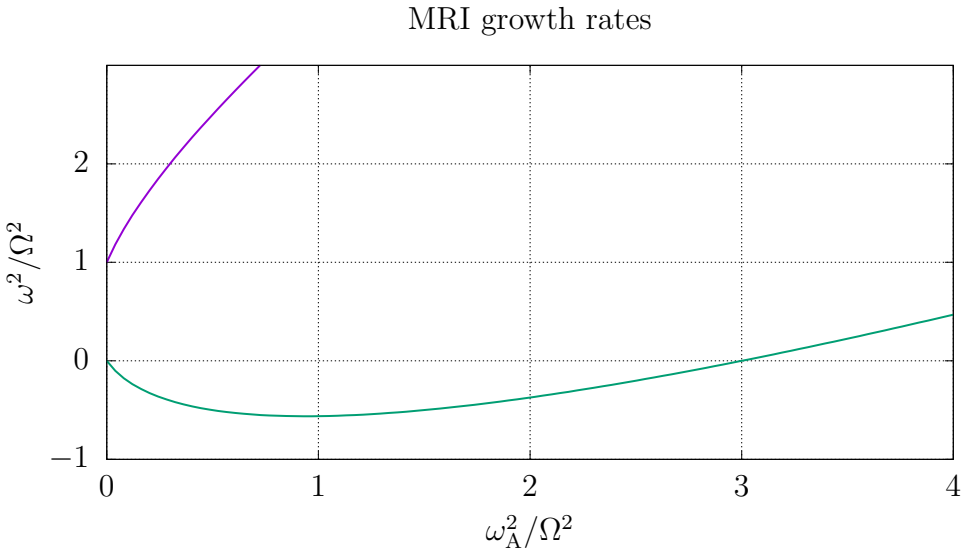

Figure 1.2: Solutions to the MRI dispersion relation with complex frequency ω plotted versus Alfvén frequency ω_A. The purple line is the stable branch while the teal line is the unstable branch, with a range of unstable modes. For $\omega_A^2/\Omega^2 > 3$, the magnetic field is strong enough that there are no longer any unstable modes.

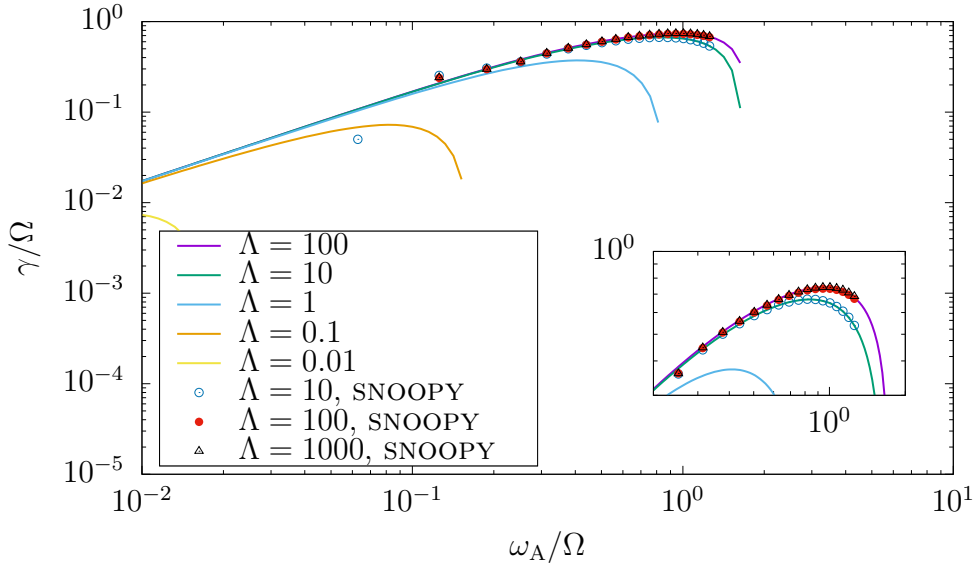

Figure 1.3: Resistive MRI growth rates γ plotted versus Alfvén frequency ω_A for solutions to the dispersion relation (lines) and numerical measurements from SNOOPY (points). For small Λ, one can see growth rates are reduced and shifted to smaller k (ω_A).

The resulting dispersion relation is

$$\omega^4 - \omega^2(\Omega^2 + 2\omega_A^2) + \omega_A^2(\omega_A^2 - 3\Omega^2) = 0. \tag{1.3}$$

Plotting the solution in Figure 1.2, we see that there are a range of unstable modes and that the fastest growing mode $\omega_{max} = 3/4\Omega$ is comparable to the rotation rate. For large ω_A, the instability is quenched by the magnetic field, which prevents bending on scales smaller than a critical scale $2\pi k_\parallel^{-1} = v_A/3\Omega$. Practically, this means that given a magnetic field, a system—real or simulated—must be thick enough to contain the MRI-unstable long-wavelength modes.

Resistive MRI

In a resistive system, the dispersion relation above is modified by the replacement $\omega \mapsto \omega_e = \omega + i\eta k^2$, introducing a new parameter the Elsasser number $\Lambda \equiv B_0^2/(\eta\Omega)$, which measures the relative strength of the resistivity. For $\Lambda \gg 1$, the growth rates are near ideal. However, for $\Lambda \leq 1$, the growth rates are reduced and the fastest growing mode is shifted toward longer wavelengths. This is important to consider when one wants to compare ideal growth rates with those from a resistive MHD simulation of the MRI. One must set the magnetic diffusivity low enough to not affect the results. See Figure 1.3 for theoretical growth rates along with those measured from fully nonlinear computations produced by the code SNOOPY, described in Section 1.5.

Azimuthal MRI

While the MRI is often discussed in the case where a vertical magnetic field component is present, Balbus and Hawley (1992) also found an instability in the case of a purely azimuthal magnetic field. This instability is particularly important for the self-generation of magnetic fields within accretion disks through a non-linear dynamo process (e.g. Rincon et al., 2007). The details of this instability are not as straightforward as the vertical case, but we will summarize. In order to consider nonaxisymmetric perturbations to the flow, one transforms to coordinates shearing with the flow

$$r' = r, \tag{1.4}$$

$$\phi' = \phi - \Omega(r)t, \tag{1.5}$$

$$z' = z. \tag{1.6}$$

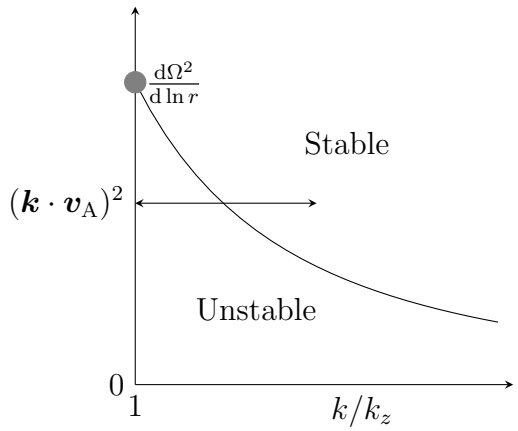

Figure 1.4: A diagram of the instability region of the azimuthal MRI (recreated from Balbus and Hawley (1992)). The field with a particular wavenumber $\boldsymbol{k}$ will experience periods of growth due a linear instability if $\boldsymbol{k}\cdot\boldsymbol{v}_\mathrm{A} < \frac{\mathrm{d}\Omega^2}{\mathrm{d}\ln r}$. Above this critical value, all solutions are stable.

Fields are expected to have the form $e^{i(k_r' r' + m'\phi' + k_z' z')}$. Therefore, the effect of the transformation is to introduce a time-dependent wavevector:

$$k_r = k_r(t) = k_r' - mt\frac{\partial\Omega}{\partial r}. \tag{1.7}$$

In this frame, the azimuthal magnetic field continually grows in time, but in such a way that $\boldsymbol{k}\cdot\boldsymbol{B}$ (both variables time-dependent) remains constant. This means that the ratio k/k_z is time-dependent.

Balbus and Hawley found that there is an unstable region of the solution space, but that the shear causes a particular wavevector to move back and forth from the stable to unstable region. While we and others will refer to this as an instability, it is actually a transient amplification, one with exponential growth over a time scale of tens of orbits. Figure 1.4 shows the instability region and the path that a wavector traces through it.

1.3 Magnetohydrodynamics

This thesis is concerned with plasmas that are well described by the fluid model of incompressible magnetohydrodynamics (MHD). While plasmas are completely described by a distribution function governed by the Vlasov-Maxwell system of equations, fluid models can be constructed from computing moments of the distribution function and making suitable approximations and closures. When the plasma is well ionized and the length scales and time scales of associated with plasma microphysics are much smaller than the scales of interest in the system, the plasma can be treated as a conducting fluid of a single species. Furthermore, for flows with characteristic frequencies much less than the inverse sound-wave crossing time, the flow can be treated as incompressible, leading to a further simplification of the equations from MHD to incompressible MHD. In the end, one has the incompressible MHD equations. They are

$$\partial_t \boldsymbol{v} = -\boldsymbol{v}\cdot\nabla\boldsymbol{v} - \frac{1}{\varrho}\nabla P + \boldsymbol{B}\cdot\nabla\boldsymbol{B} + \nu\nabla^2\boldsymbol{v} + \boldsymbol{f}, \tag{1.8}$$

$$\partial_t \boldsymbol{B} = \nabla\times(\boldsymbol{v}\times\boldsymbol{B}) + \eta\nabla^2\boldsymbol{B} + \boldsymbol{g}, \tag{1.9}$$

$$\nabla\cdot\boldsymbol{v} = 0, \quad \nabla\cdot\boldsymbol{B} = 0, \tag{1.10}$$

where $\boldsymbol{v}$ is the velocity, $\boldsymbol{B}$ is the magnetic field in velocity units,[2] P is the total pressure,[3] ν is the kinematic viscosity, η is the magnetic diffusivity, and $\boldsymbol{g}, \boldsymbol{f}$ are generic forcing functions.

[2] One can define the Alfvén speed $v_\mathrm{A} \equiv \frac{B}{\sqrt{4\pi\varrho}}$ and use this as the unit of the magnetic field.

[3] We can redefine the pressure as $P \equiv p + B^2/4\pi$ for the *incompressible* MHD equations because the divergence of the first equation gives you Laplace's equation for P

$$0 = \nabla^2 P = \nabla^2\left(p + \frac{B^2}{4\pi}\right) \tag{1.11}$$

where the role of the fluid pressure p is to adjust itself so that this equation is always satisfied. Because p never enters the dynamical equations by itself, the values of the fluid and magnetic pressure terms individually are irrelevant.

Hydrodynamic turbulence

The most studied turbulent system and that from which the plasma community has drawn much intuition is that of hydrodynamic turbulence. Concepts such as the cascades of ideally conserved quantities like energy, correlated flow structures known as "eddies," and intermittency were borrowed from the hydrodynamics community (e.g., Richardson, 1922; Frisch, 1995).

Magnetohydrodynamic turbulence

Magnetohydrodynamic turbulence shares similarities with its hydro counterpart, including a forward cascade of energy and an inertial range with a constant energy transfer rate. However, it differs in many key components. Without the presence of a magnetic field, one can perform a Galilean transformation of the coordinates to a frame with zero mean velocity where the fluctuations of the flow are distributed isotropically. This is not possible with a magnetic field, and this symmetry breaking provides a preferred direction for the system. Along the magnetic field direction, shear Alfvén waves propagate and interact, bending the field lines as if they were strings under tension. These waves are the building blocks of MHD turbulence.

By introducing the Elsasser variables $\boldsymbol{z}^{\pm} = \boldsymbol{v} \pm \boldsymbol{B}$, one can transform the MHD equations to the form

$$\partial_t \boldsymbol{z}^{\pm} \mp \boldsymbol{v}_{\mathrm{A}} \cdot \nabla \boldsymbol{z}^{\pm} + \boldsymbol{z}^{\mp} \cdot \nabla \boldsymbol{z}^{\pm} = -\nabla P + \frac{\nu + \eta}{2} \nabla^2 \boldsymbol{z}^{\pm}, \tag{1.12}$$

$$\nabla \cdot \boldsymbol{z}^{\pm} = 0. \tag{1.13}$$

One can see from the equations that $\boldsymbol{z}^{\pm}$ nonlinearly couples only with $\boldsymbol{z}^{\mp}$. Because $\boldsymbol{z}^{\pm}$ correspond to Alfvén waves that are propagating or counter-propagating along the magnetic field direction, only waves that are propagating in opposite directions can interact with each other.

Magnetohydrodynamic turbulence phenomenology

Since Kolmogorov's landmark papers (Kolmogorov, 1941a,b, 1962) on hydrodynamic turbulence, several phenomenological models for the inertial range of MHD have been proposed. The common feature of these models is that by neglecting the dissipation and forcing terms in the equations, one has an equation that describes the flow on scales between where the energy is injected and where it is removed. This "inertial range" is dominated by the inertial terms in the equations. By assuming a constant energy transfer rate through all scales, one can obtain the dependence of velocity and magnetic field fluctuations $\delta v_\lambda, \delta b_\lambda$ on the scale λ. The particular form of the dependence is determined by the model.

Iroshnikov (1963) and Kraichnan (1965) proposed a model of weak[4] turbulence in which an "eddy" (correlated δv_λ and δb_λ) is distorted by counter-propagating eddies over the course of many interactions. One can estimate the change from one interaction in the Iroshnikov-Kraichnan (IK) model by assuming that the eddy decorrelates on the field-parallel length scale λ. Then, equation 1.12 gives the estimate $\Delta\delta v_\lambda \sim (\delta v_\lambda^2/\lambda)(\lambda/\delta v_\lambda)$. Because these are disturbances are assumed random, many interactions are required to remove the energy of an eddy, transferring it to smaller scales, specifically $N \sim (\delta v_\lambda/\Delta\delta v_\lambda)^2$. A energy transfer time can be estimated by finding the time for N individual interactions

$$\tau_{\rm IK} \sim N\lambda/v_{\rm A} \sim \lambda/\delta v_\lambda(v_{\rm A}/\delta v_\lambda). \tag{1.14}$$

A constant energy transfer rate $\delta v_\lambda^2/\lambda$ produces fluctuations $\delta v_\lambda \propto \lambda^{1/4}$ and the energy spectrum

$$E_{\rm IK}(k) = |\delta v_k^2|k^2 \propto k^{-3/2}. \tag{1.15}$$

[4] $\delta v \sim \delta b \ll v_{\rm A}$

In light of results for systems with weaker magnetic fields that indicate an energy spectrum closer to the Kolmogorov $E(k) \propto k^{-5/3}$, Goldreich and Sridhar (1995) (GS95) developed a framework that accounts for the anisotropy produced by the presence of a magnetic field. They introduced the concept of "critical balance" wherein the nonlinear and linear advection terms are balanced $|\boldsymbol{v}_\mathrm{A} \cdot \nabla \boldsymbol{z}^\pm| \sim |\boldsymbol{z}^\mp \cdot \nabla \boldsymbol{z}^\pm|$. This is also a consequence of causality: information about a perpendicular disturbance δb_λ can only be propagated a distance $l \sim v_\mathrm{A} \delta b_\lambda / \lambda$ along a magnetic field line.

It is worth noting here that the GS95 theory is a theory of strong turbulence, in contrast with IK theory. In fact, Sridhar and Goldreich (1994) and others (Montgomery and Matthaeus, 1995; Ng and Bhattacharjee, 1996; Goldreich and Sridhar, 1997; Galtier et al., 2000) realized that not only was IK theory formally inconsistent with strong turbulence, by assumption, but also it failed as a description of weak turbulence. Ultimately, the energy spectrum was shown to be $E(k_\perp) \sim k^{-2}$.

While systems with weaker magnetic fields exhibited the GS95 spectrum, those with a strong field were closer the IK spectrum. Motivated by this discrepancy, Boldyrev (2005, 2006) introduced a model that in the limit of strong guide field reproduces the energy spectrum scaling of IK. In this model, anisotropic turbulent eddies have three characteristic scales—compared to two in GS95 and one in IK—and "scale-dependent dynamic alignment" governs the strength of the nonlinear interaction. An eddy δb_λ, of length l and transverse scale λ, distorts the magnetic field lines by an amount $\xi \propto \delta b_\lambda l$, and these three scales become the length, thickness, and width, respectively, of an eddy. The alignment of velocity and magnetic perturbations is given by the ratio of these last two scales $\theta_\lambda \sim \lambda / \xi$. By assuming that the the eddies try to maximally align δv_λ and δb_λ at each scale, the resulting alignment angle scales as $\theta_\lambda \sim \lambda^{1/4}$ Consequently, there

is greater alignment at smaller scales, and the eddy dimensions scale as

$$l \sim \lambda^{1/2}, \tag{1.16}$$

$$\xi \sim \lambda^{3/4}, \tag{1.17}$$

Velocity fluctuations then scale as $\delta v_\lambda \sim \lambda^{1/4}$, producing an energy spectrum

$$E(k_\perp) \propto k_\perp^{-3/2}, \tag{1.18}$$

where $k_\perp$ is the wavenumber in the plane perpendicular to the magnetic field.

A consequence of the dynamic-alignment (DA) theory is that eddies become progressively more ribbon-like at smaller scales, indicating that strong[5] MHD turbulence tends to produce current sheets. This is unlike hydrodynamic turbulence which creates not vortex sheets but filaments (e.g., Biskamp, 2003; Maron and Goldreich, 2001; Mallet et al., 2016). These current sheets will be the sites of energy dissipation, with a log-normal model describing well the intermittent process Zhdankin et al. (2013, 2014). If the inertial range is long enough, i.e. the Lundquist number is large, then these current sheets can become unstable to the tearing mode before reaching the dissipation range.

In order to resolve this consequence of DA theory, Loureiro and Boldyrev (2017) and Mallet et al. (2017a) separately developed phenomenological theories that describe this "tearing-mediated" regime. They propose a new range that exists between a critical "disruption" scale $\lambda_{\rm cr} \sim S_L^{-4/7}$ and a new dissipation scale $\lambda_{\rm c} \sim S_L^{-6/7}$, where S_L is the Lundquist number associated with an outer scale L. The disruption scale is found by equating the tearing time and nonlinear interaction time, and the dissipation scale is set by the critical Lundquist number at which a current sheet becomes

[5] "Strong" here refers to turbulence that is critically balanced at the outer scale and, therefore, all smaller scales.

violently unstable to the plasmoid instability Loureiro et al. (2007). As the tearing mode tends to create isotropic magnetic field structures from magnetic shear, Boldyrev and Loureiro (2017) predict that the turbulence becomes progressively less aligned at smaller scales.

The exact scaling of the energy spectrum and alignment depend on a parameter within the model and on what shape one assumes for the current sheets, either hyperbolic-tangent shaped or sine shaped (Boldyrev and Loureiro, 2017). Whatever the details, the spectrum becomes steeper and the alignment increases at smaller scales.

Numerical studies of MHD turbulence have previously been used to identify the properties associated with inertial range of DA turbulence (e.g., Perez and Boldyrev, 2010a; Mason et al., 2012; Perez et al., 2014b) However, the Lundquist number necessary to observe this tearing-mediated regime is roughly $S_L \gg 10^7$, which is currently prohibitive for fully three-dimensional computations. Two-dimensional setups provide the best hope at this point for testing this theory. Our work on this problem (Walker et al., 2018)—presented in an extended form in this thesis—and that of Dong et al. (2018) both reported results that displayed some of the characteristics predicted by the theory. These included the measuring power laws with spectral indices close to theoretical predictions, as well qualitative features such as extended current sheet structures with plasmoid chains.

Finally, let us note that in this thesis we may at times use the terminology "standard MHD turbulence" to refer to the well-studied setup comprising incompressible MHD with strong guide field (B_0), randomly forced such that $B_0/B_{\rm rms} \geq 5$ and $v_{\rm rms} \sim B_{\rm rms} \sim v_{\rm A}$. This setup produces strong turbulence exhibiting the characteristics of the DA theory and will be the benchmark to which other systems are compared.

1.4 Shearing Box

Parts of this dissertation will be concerned with the numerical simulation of local accretion disk turbulence as described by MHD and the so-called "shearing-box" approximation. This approximation allows the local properties of turbulence in the mid-plane of the disk to be studied while neglecting large-scale effects such as stratification and stream-line curvature (Goldreich and Lynden-Bell, 1965; Hawley et al., 1995; Umurhan and Regev, 2004; Fromang et al., 2007; Longaretti and Lesur, 2010; Lesur and Longaretti, 2011; Riols et al., 2015). The dynamics studied in the shearing box are therefore not only applicable to accretion disks but also to other astrophysical and laboratory systems possessing rotating, shearing flows (e.g., Kagan and Wheeler, 2014; Petitdemange et al., 2008; Ji and Balbus, 2013).

A summary of this model will be given, along with references to derivations in the literature. First we will summarize the results, and then we will derive them in later sections.

One expands linearly in the ratio of box width Δ to fiducial radius r_o of a point in the disk to construct a small box rotating with the flow. By keeping only linear terms in Δ/r_0, curvature is ignored, and the Cartesian coordinates of the this box correspond to global coordinates by

$$\hat{\boldsymbol{r}} \to \hat{\boldsymbol{x}}, \quad \hat{\boldsymbol{\phi}} \to \hat{\boldsymbol{y}}, \quad \hat{\boldsymbol{z}} \to \hat{\boldsymbol{z}}. \tag{1.19}$$

A system of equations is obtained for deviations $\boldsymbol{v}$ from a steady background flow

$$D_t \boldsymbol{v} = -\boldsymbol{v} \cdot \nabla \boldsymbol{v} - \frac{1}{\varrho} \nabla P + \boldsymbol{B} \cdot \nabla \boldsymbol{B} + \nu \nabla^2 \boldsymbol{v} - 2\boldsymbol{\Omega}_0 \times \boldsymbol{v} + q\Omega_0 v_x \hat{\boldsymbol{y}}, \tag{1.20}$$

$$D_t \boldsymbol{B} = \boldsymbol{\nabla} \times (\boldsymbol{v} \times \boldsymbol{B}) + \eta \nabla^2 \boldsymbol{B} - q\Omega_0 B_x \hat{\boldsymbol{y}}, \tag{1.21}$$

$$\nabla \cdot \boldsymbol{v} = 0, \tag{1.22}$$

$$\nabla \cdot \boldsymbol{B} = 0, \tag{1.23}$$

where $D_t \equiv \partial_t - q\Omega_0 x \partial_y$ is the modified time derivative due to the background flow, $\boldsymbol{\Omega}_0 = \Omega_0 \hat{\boldsymbol{z}} = \Omega(r_0)\hat{\boldsymbol{z}}$ is the angular velocity at the fiducial radius, and q is the shearing rate (equal to 3/2 in Keplerian disks).

The shearing rate is defined by the parameter

$$q \equiv -\left(\frac{\mathrm{d}\ln\Omega(r)}{\mathrm{d}\ln r}\right)_{r_0} = \frac{2A}{\Omega_0}, \tag{1.24}$$

where A is the Oort constant, and $\Omega_0 = \Omega_K(r_0)$ is the Keplerian angular velocity at r_0.

Derivation of shearing box equations

We start from the MHD equations for a Cartesian box in a Keplerian orbit,

$$\frac{\partial \boldsymbol{u}}{\partial t} + \boldsymbol{u}\cdot\nabla\boldsymbol{u} = -\frac{1}{\varrho}\nabla P + \boldsymbol{B}\cdot\nabla\boldsymbol{B} + \nu\nabla^2\boldsymbol{u} - 2\boldsymbol{\Omega}_0\times\boldsymbol{u} + 2q\Omega_0^2 x\hat{\boldsymbol{x}}, \tag{1.25}$$

$$\frac{\partial \boldsymbol{B}}{\partial t} + \boldsymbol{u}\cdot\nabla\boldsymbol{B} - \boldsymbol{B}\cdot\nabla\boldsymbol{u} = \eta\nabla^2\boldsymbol{B}, \tag{1.26}$$

notating that the last two terms of equation 1.25 are the Coriolis and centrifugal terms, respectively. These appear because the box represents a non-inertial, rotating frame. Identifying that a steady solution $\boldsymbol{w} = -q\Omega_0 x\hat{\boldsymbol{y}}$ exists, we make the substitution $\boldsymbol{u} = \boldsymbol{w} + \boldsymbol{v} = -q\Omega_0 x\hat{\boldsymbol{y}} + \boldsymbol{v}$ to get equations 1.20 and 1.21. To eliminate the explicit spatial dependence, we transform to shearing coordinates defined by:

$$t' = t, \quad X = x, \quad Y = y - q\Omega_0 x t, \quad z = z, \tag{1.27}$$

$$\frac{\partial}{\partial t} = \frac{\partial}{\partial t'} - q\Omega X\frac{\partial}{\partial Y}, \quad \frac{\partial}{\partial x} = \frac{\partial}{\partial X} - q\Omega t'\frac{\partial}{\partial Y}, \quad \frac{\partial}{\partial y} = \frac{\partial}{\partial Y}, \quad \frac{\partial}{\partial z} = \frac{\partial}{\partial Z}. \tag{1.28}$$

and make the identification $\nabla' - q\Omega t\frac{\partial}{\partial Y}\hat{\boldsymbol{x}} \to \nabla(t)$. This produces a set of equations that is equivalent to incompressible MHD with Coriolis and shear,

with a time-dependent gradient,

$$\frac{\partial \boldsymbol{u}}{\partial t'} + \boldsymbol{u}\cdot\nabla'\boldsymbol{u} - St' u_X \frac{\partial}{\partial Y}\boldsymbol{u} = -\frac{1}{\varrho}(\nabla' - St'\frac{\partial}{\partial Y})P \tag{1.29}$$

$$+ \boldsymbol{B}\cdot\nabla'\boldsymbol{B} + \nu\nabla'^2\boldsymbol{u} - 2\boldsymbol{\Omega}_0\times\boldsymbol{u} - Su_X\hat{\boldsymbol{y}}, \tag{1.30}$$

$$\frac{\partial \boldsymbol{B}}{\partial t'} + \boldsymbol{u}\cdot\nabla'\boldsymbol{B} - \boldsymbol{B}\cdot\nabla'\boldsymbol{u} = \eta\nabla'^2\boldsymbol{B}, \tag{1.31}$$

where $S = -q\Omega_0$.

In this shearing frame, the coordinates (X, Y, Z) are periodic, but now the derivatives are time-dependent. We would like to remove the terms that explicitly depend on time. Because all field are now periodic in the (X, Y, Z) frame, one can simply express each through a Fourier expansion in the new phase space $\boldsymbol{k'} = (k_X, k_Y, k_Z)$. For example, the scalar variable ξ would have the expansion

$$\xi(\boldsymbol{X}) = \sum_{\boldsymbol{k'}} \xi_{\boldsymbol{k'}} e^{i\boldsymbol{k'}\cdot\boldsymbol{X}}, \tag{1.32a}$$

$$= \sum_{\boldsymbol{k(t)}} \xi_{\boldsymbol{k}(t)} e^{i\boldsymbol{k}(t)\cdot\boldsymbol{x}}. \tag{1.32b}$$

This relation implicitly defines the time-dependent wavevectors,

$$k_x(t) = k_X - q\Omega t k_Y, \tag{1.33a}$$

$$k_y = k_Y, \tag{1.33b}$$

$$k_z = k_Z. \tag{1.33c}$$

The key step to removing the time-dependent terms from Eq. 1.30 is to use the expansions in Eq.1.33. There are two equivalant ways of doing this. The first is to use Eq. 1.32a directly and then collect the terms $k_x(t) = k_X - Stk_Y$. The second is to use Eq. 1.32b, which is an expansion with respect to the unsheared coordinates and formally transform back to the unsheared coordinates by the substitution $\nabla' - St'\frac{\partial}{\partial Y}\hat{\boldsymbol{x}} \to \nabla$.

A consequence of this representation is that any mode of a field with nonzero k_y will gradually shift in k_x due to the shear. If continued indefinitely, large-scale structures will be sheared until they reach the dissipation scale. Instead, a remapping procedure is applied that periodically remaps the fields in order to continue resolving these structures.

Remapping procedure

In order to continue resolving large-scale structures that would be sheared away due to finite resolution, a periodic remapping of the fields is performed. Let us explain this procedure and its rationale.[6]

Consider a structure concentrated in phase space of the non-shearing coordinates (x, y) around some mode $(k_x, k_y) = (l, m)$ at t_0. We can transform to the shearing frame $\xi(x, y, t) \to \xi(X, Y, T)$, where $T = t - t_0$ is the time in the shearing frame the reference time t_0. This transformation results in the relation

$$\xi(x, y, t) = \xi_{l,m} e^{ilx+imy} = \xi_{l,m} e^{i(l-STm)X+imY} = \xi(X, Y, T). \tag{1.34}$$

At $T = 0$, the amplitude $\xi_{l,m}$ corresponds to the same mode in either frame. In the shearing frame, at some later time T, the energy has been transferred to a mode $(k_X, k_Y) = (l - STm, m)$. We see that this wavenumber grows without bound as T.

For a given resolution N_x, the maximum wavenumber that can be represented is $k_{\max} = N_x/2 - 1$. Therefore, a mode (k_0, m) can be resolved for maximum time of

$$T_{\text{res}} = \frac{k_{\max}}{S|m|} + \frac{l}{Sm}. \tag{1.35}$$

In other words, information will be permanently lost due to the shearing coordinates after a time T_{res}.

[6] See also Umurhan and Regev (2004) for a detailed explanation.

This can be prevented by noting that after a remap time $T_{\rm rm}$ in the sheared frame, we can map back to the unsheared frame by the inverse transformation of Eq. 1.34

$$\xi(X, Y, T_{\rm rm}) \rightarrow \xi(x, y, t_0 + T_{\rm rm}). \tag{1.36}$$

That is the information that was initially in (l, m) has been remapped to that position. Now, we reset the refrence time $t_0 \rightarrow t_0 + T_{\rm rm} = t_0'$, reset $T = t - t_0'$ and map back

$$\xi(x, y, t_0') \rightarrow \xi(X, Y, T). \tag{1.37}$$

The choice of this remap time is arbitrary, but there is natural choice in choosing the time when the box is exactly periodic with respect to the non-sheared coordinates, that is

$$T_{\rm rm} = \left| \frac{L_y}{S L_x} \right| \tag{1.38}$$

For a well-resolved simulation, high m modes are sitting in the dissipation range anyway, or in the anti-aliasing cutoff regime. The primary is concern is how to continue resolving modes at the largest scales (low l_0). This choice of remap time does that.

Domain of applicability

The shearing-box approximation is local in nature. By using periodic boundary conditions, one is assuming that the domain is not interacting with any nearby elements of the disk. Obviously, this will only hold for short time and length scales. The units of time, length, and velocity are the inverse angular frequency $\tau = \Omega_0^{-1}$, box size L, and orbit velocity $v_0 = L\Omega_0$, respectively. This means that the crossing time of the box is the box width

divided by typical radial (x) velocity $v_{x,\mathrm{rms}}$, $L/v_{x,\mathrm{rms}} \sim \tau$. Based upon this, one might say that using the shearing-box for times longer than τ is unphysical because the box would have interacted with its environment after this amount of time. However, for steady-state runs where averages are taken over the course of a long simulation, one is not simulating the long-time behavior of the turbulence. One is gathering data for statistical analysis of the short-time behavior of turbulence in such a system. It is useful to think of the steady-state shearing-box simulations of disk turbulence as an ensemble of different instances of local, MRI-generated turbulence.

Conservation laws

It is instructive to compare the conservation laws of Equations (1.8)-(1.9), with those of MHD. In non-rotating systems, the incompressible MHD equations conserve the quadratic integrals of energy, cross helicity, and magnetic helicity if external energy supply and energy dissipation are absent (e.g., Biskamp, 2003; Tobias et al., 2013). In the shearing-box model, energy is supplied to the system by the instability and through the turbulent Reynolds and Maxwell stresses. This energy is sourced from the background shear and, in disks, ultimately from gravity. From Eqs. 1.20 and 1.21 one then derives for the energy Eq. 2.3

$$\frac{d}{dt}\left\langle \frac{v^2}{2} + \frac{B^2}{2} \right\rangle = q\langle v_x v_y - B_x B_y \rangle - \nu\langle \omega^2 \rangle - \eta\langle j^2 \rangle, \tag{1.39}$$

where the angular brackets denote a spatial average over the domain. The conservation law of cross helicity has to be modified in the shearing box as

$$\frac{d}{dt}\langle \boldsymbol{v} \cdot \boldsymbol{B} \rangle = (q-2)\langle \boldsymbol{\Omega}_0 \cdot \boldsymbol{A} \rangle - (\nu+\eta)\langle \boldsymbol{\omega} \cdot \boldsymbol{j} \rangle, \tag{1.40}$$

while the conservation law for magnetic helicity remains unchanged:

$$\frac{d}{dt}\langle \boldsymbol{B} \cdot \boldsymbol{A} \rangle = -2\eta \langle j^2 \rangle. \tag{1.41}$$

In these equations we introduce the vorticity $\boldsymbol{\omega} = \nabla \times \boldsymbol{v}$, the current density $\boldsymbol{j} = \nabla \times \boldsymbol{B}$, and the vector potential $\boldsymbol{A}$, where $\boldsymbol{B} = \nabla \times vecA$. In the presence of the magnetorotational instability and in the absence of dissipation, the energy grows while the cross helicity and magnetic helicity do not. Note, the cross helicity becomes gauge-dependent, like the magnetic helicity.

1.5 Numerical method

Snoopy

All of the computational results presented in this thesis were produced by the publicly available code SNOOPY written by Geoffroy Lesur (Lesur and Longaretti, 2007). It uses a pseudospectral method to represent functions on a Cartesian grid using a Fourier basis in two or three dimensions. Time integration is performed by a low-storage third-order Runga-Kutta scheme, and dissipation terms are handled implicitly. By default, fields are fully dealiased using the "3/2-rule"(Canuto et al., 2006). Transforms are handled by the FFTW3 library (Frigo and Johnson, 2005), and parallelization is achieved using the Message Passing Interface (MPI) and OpenMP standards.

SNOOPY solves the compressible MHD equations with additional effects included modularly, such as rotation, shear, and Hall effect. In particular, the code implements the shearing-box model by solving equations in the shearing frame. As discussed in Umurhan and Regev (2004), the flow needs to be periodically remapped inside the shearing box in order to prevent large-scale structures from being sheared to such small wavenumbers that they are no longer effectively resolved. SNOOPY carefully performs this remap

procedure so that minimal energy is lost when the flow is fully resolved. In other words, zeroed wavenumbers are deep in the dissipation range.

The work of this thesis employs incompressible MHD, with and without several of the effects listed above. Each specific section will note which equations are being solved, in how many dimensions, etc. Note, both velocity and magnetic field are represented in velocity units.

1.6 Thesis outline

The remainder of the thesis is organized as follows. Chapter 2 will present our work on turbulence driven by the linear MRI in the case where a net, magnetic flux is present in the system. Chapter 3 contains the analysis of our computational results on zero-net-flux shearing-box simulations of the MRI dynamo. Chapter 4 examines results of our model of simulating tearing-mediated turbulence through the use of a two-dimensional, critically balanced eddy. Finally, Chapter 5 will summarize the results and discuss potential future research avenues.

2 MRI-DRIVEN TURBULENCE: NET FLUX

Prior numerical studies of the shearing-box model revealed nontrivial properties of the resulting magnetic turbulence. In the case of zero net magnetic flux through the system, it was found that turbulence was sustained for magnetic Prandtl numbers exceeding unity, while it was observed to eventually decay for smaller values (Fromang et al., 2007; Balbus and Henri, 2008; Riols et al., 2013, 2015). Larger Reynolds numbers seem to facilitate the MRI dynamo action by lowering the Prandtl number threshold, however, present numerical limitations do not allow one to establish whether this dependence persists at asymptotically large Reynolds numbers. In the case of nonzero net magnetic flux, it was found that the steady state is eventually reached that depends on the value of the flux and also on the magnetic Prandtl number (Longaretti and Lesur, 2010).

In order to understand the behavior exhibited by numerical simulations, it is instructive to understand the properties of the magnetic turbulence that develops in the system. This the goal of the present chapter, which presents in an extended form the results of Walker et al. (2016). It was motivated by several puzzling results obtained in previous works. In particular, previous studies did not find a power-law scaling of the energy spectrum of magnetorotational turbulence (Lesur and Longaretti, 2011). It remained unknown whether such a system develops a turbulent cascade similar to that found in forced MHD turbulence (e.g., Perez et al., 2012; Mason et al., 2012), and whether there is any universality among the turbulent states corresponding to different parameter regimes.

As discussed in Section 1.3, MHD turbulence is characterized by highly anisotropic eddies at scales λ much smaller than the driving scale L. The anisotropy is three-dimensional. One dimension l (length) is along the guide field, whether that be a strong constant field or some large scale field that appears locally constant. The other two dimensions λ, ξ (thickness and

width, respectively) are in a plane perpendicular to the guide field. For a fully developed turbulent flow comprising many eddies, the distribution of these fluctuations is isotropic in the perpendicular plane; that is, there is no preferred direction. Therefore, one typically considers the energy spectrum of strong, driven MHD turbulence as a function of parallel and perpendicular wavenumbers, i.e. $E = E(k_\parallel, k_\perp)$. When you have a system that has three distinct directions at all scales, reflected in the shear and Coriolis terms, it is not a priori clear that the turbulence that develops will have the same characteristics as it would without these effects.

We have found that in the cases when a steady or quasi-steady turbulent field is observed, it develops two distinct components. The first component consists of strong magnetic fluctuations, almost in the direction of the shear. The spectrum of this component declines as k^{-2}; therefore, this component is concentrated at large scales. The remainder of the fluctuations comprise the second, small-scale component that exhibits a turbulent cascade with the shallower spectrum of $-3/2$, similar to that of standard MHD turbulence. The large-scale component of the turbulence plays the role of the guide field for the small-scale component. We observe that the intensity of the resulting turbulence depends on the net magnetic flux. However, there is remarkable universality among all the observed turbulent regimes—the level of turbulence and its outer scale are adjusted in such a way as to ensure that the rate of non-linear interaction is proportional to the shear rate of the background flow.

In this chapter we will present results from shearing-box simulations of MRI-driven turbulence, compare them with those from standard MHD turbulence and DA theory, and present a phenomenological picture that explains the observations. Section 2.1 will describe the setup used. Section 2.2 will present the numerical results. Section 2.3 will propose a phenomenological picture. Finally, Section 2.4 will provide conclusions and a discussion.

2.1 Methodology

We use the shearing-box approximation as described in Section 1.4, with the parameters $\Omega_0 = 1, q = 3/2, \varrho = 1$, for the rotation rate, shear, and density, respectively. The variables are non-dimensionalized using the inverse of the rotation rate of the disk $t_0 = \Omega_0^{-1}$ as the unit of time, the box height L_z as the unit of length, $\Omega_0 L_z$ as the unit of velocity. The magnetic field B will be expressed in velocity units. We will consider systems with an imposed uniform field $\boldsymbol{B}_0 = B_0\hat{\boldsymbol{z}}$, and define the fluctuating part of the magnetic field $\boldsymbol{b}$ according to $\boldsymbol{B} = \boldsymbol{B}_0 + \boldsymbol{b}$.

The relevant dimensionless quantities are the Reynolds number $\mathrm{Re} = \Omega_0 L_z^2/\nu$, the magnetic Reynolds number $\mathrm{Rm} = \Omega_0 L_z^2/\eta$, the Elsasser number $\Lambda_\eta = B_0^2/\Omega_0\eta$, and the parameter $\beta = \Omega_0^2 L_z^2/B_0^2$, which measures the strength of the imposed magnetic field and mimics the plasma β in vertically stratified disks. The Reynolds numbers are chosen to be equal so that the magnetic Prandtl number $\mathrm{Pm} = \nu/\eta$ is unity. We also introduce the dimensionless transport coefficient

$$\alpha \equiv \langle v_x v_y - b_x b_y \rangle / \Omega_0^2 L_z^2, \tag{2.1}$$

and the energy injection rate

$$\tilde{\alpha} \equiv q\langle v_x v_y - b_x b_y \rangle, \tag{2.2}$$

where $\langle\cdot\rangle$ denotes an average performed over the entire volume. From Eqs. 1.20 and 1.21, the energy balance equation has the form (Longaretti and Lesur, 2010):

$$\frac{d}{dt}\left\langle \frac{v^2}{2} + \frac{b^2}{2} \right\rangle = -\nu\big\langle (\nabla \times \boldsymbol{v})^2 \big\rangle - \eta\big\langle (\nabla \times \boldsymbol{b})^2 \big\rangle + \tilde{\alpha}. \tag{2.3}$$

In this work, we consider the simulation box with dimensions $(L_x, L_y, L_z) =$

$(2, 4, 1)$[1] and numerical resolution of $N_x \times N_y \times N_z = 1024 \times 1024 \times 512$. All cases have a kinematic viscosity $\nu = 1/45000$ such that the nominal Reynolds number is $\mathrm{Re} = 45000$. Each setup is then evolved over approximately $50t_0$ to achieve a steady state from which to calculate averages of various quantities. We will consider three steady-state net-flux cases and one zero-net-flux case. The latter will be discussed more in Chapter 3, but it will be illustrative to consider this setup when understanding the level of saturation and outer scale of the turbulence in the net-flux setups.

Case I has a mean field of $B_0 = 0.03$, corresponding to $\beta \approx 1100$. The initial conditions are large-scale random fluctuations in both $\boldsymbol{v}$ and $\boldsymbol{B}$. Case I is this steady state after the initial growth period, with averages performed over the final approximately $50t_0$.

Case II is another steady-state case that has a weaker mean field of $B_0 = 0.010$ and used a snapshot of Case I as its initial condition. After the steady state was reached, averages were performed over the final approximately $20t_0$.

Case III corresponds to a very weak net flux of $B_0 = 0.005$. To initiate this run, the a magnetic field was added to the simulations of our zero-net-flux setup—Case IV below—such that $\Lambda_\eta \approx 1$. This was so that the linear MRI, which is quenched at high wavenumbers for $\Lambda_\eta < 1$, would be excited with a minimal injection of energy. We observe that the turbulence reaches a new, lower-energy steady state in this case. Averages were performed over the final approximately $100t_0$.

Case IV is a zero-net-flux case that used as its initial condition a snapshot of Case I in which the mean field was manually zeroed. This initial condition was chosen in order to kill the linear MRI but begin with a fully turbulent state. We observe that in this case the energy declines very slowly, on the

[1] Bodo et al. (2008) showed that boxes with $L_x > L_z$ will allow more "parasitic modes" (secondary instabilities) that feed off of the primary MRI "channel mode" and control saturation Therefore a box elongated in the radial direction will not include channel mode solutions that saturate at unphysically high amplitudes. In Chapter 3, we will explore the effects of changing the aspect ratio in the case of zero net flux.

Case	B_0	$n_{\max}$	n_{cut}	n_{alias}	Λ_η
I	0.030	5.1	9	170	40.5
II	0.010	15.4	27	170	4.5
III	0.005	30.8	55	170	1.125

Table 2.1: Linearly unstable MRI modes for cases I, II, and III. Unstable modes range from $n = 1$ to n_{cut}, with the fastest growing (ideal) mode at $n_{\max}$, where $n = k_z \frac{L_z}{2\pi}$. Due to dealiasing, the highest mode represented by the grid is n_{alias}.

time scale of about $100t_0$, consistent with the fact that the energy injection and dissipation rates nearly balance each other (see Fig. 2.1). This suggests that the role of the imposed field and the associated magnetorotational instability in the steady-state Cases I-III is merely to compensate for the very slight mismatch between the non-linear energy injection and dissipation rates.

We note that each setup includes a range of linearly unstable MRI modes near the fastest growing mode. While this is true for Cases II and III, the growth rates are reduced and the maximal wavenumber is shifted because of the small value of Λ_η (see Sec. 1.2). These properties of the linear MRI for each setup are gathered in Table 2.1.

2.2 Results

In all turbulent states, the spectra of total energy do not display good power-law scaling (see, e.g., Fig. 2.2). This is consistent with previous studies (e.g., Fromang, 2010; Lesur and Longaretti, 2011), where it was also found that while the total energy spectrum does not have good scaling, the kinetic spectrum exhibits the scaling somewhat close to $k^{-3/2}$.

We find, however, that a more informative analysis can be performed if the field b_y is separated from the total energy spectrum. As seen in Fig. 2.3, the energy in b_y is larger than in the rest of the fields; it is peaked

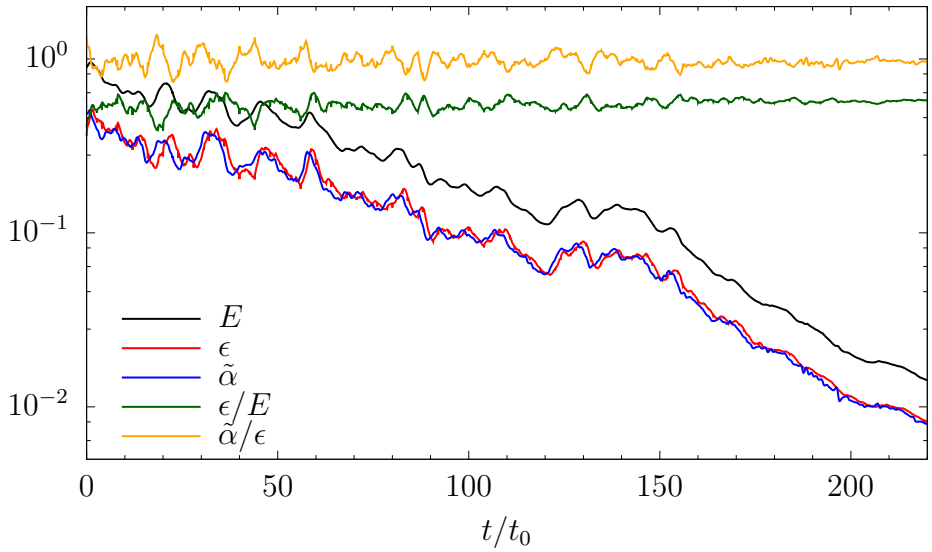

Figure 2.1: Time history of Case IV showing energy E, energy injection rate $\tilde{\alpha}$, and energy dissipation rate ϵ.

at large scales and it rapidly declines with decreasing scale. Indeed, due to the Ω-effect, fluctuations of magnetic field in a sheared flow become more aligned with the shear, enhancing the strength of the field in the shear direction (see Fig. 2.4). The energy spectrum of the b_y fields scales closely to k^{-2} which is possibly related to the domain structure seen in Fig. 2.4, with sharp boundaries between the domains where the direction of the field reverses[2].

The large-scale field b_y is also responsible for the energy supply through the Maxwell stress $\langle b_x b_y \rangle$. This stress dominates over the Reynolds stress $\langle v_x v_y \rangle$, while both are concentrated at large scales (see Figs. 2.5 and 2.6). In the latter figure, we define the cumulative energy injection function as

$$C(k) = \frac{\int_k^\infty \tilde{\alpha}(k)dk}{\int_1^\infty \tilde{\alpha}(k)dk}, \tag{2.4}$$

[2]The Fourier spectrum of a step function goes as k^{-2}.

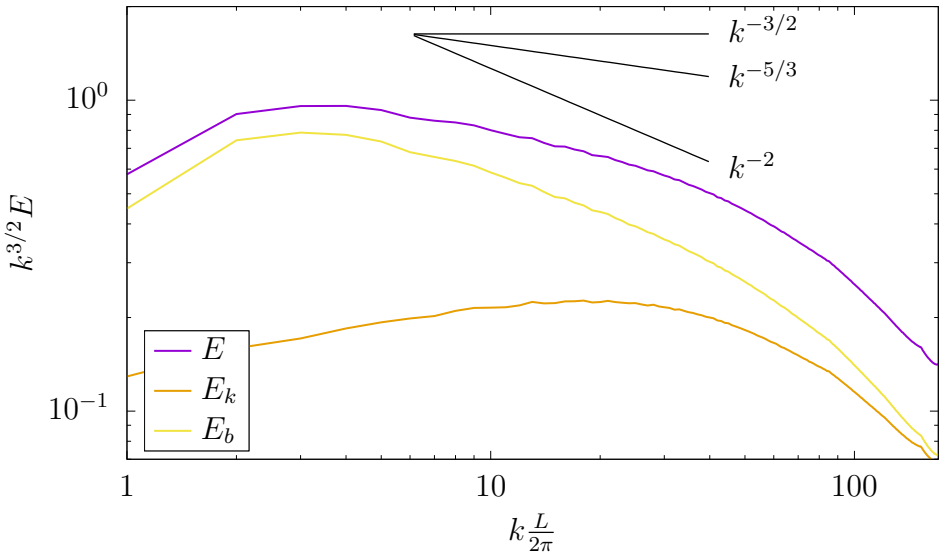

Figure 2.2: From Case I, energy spectra for the total energy, kinetic energy, and magnetic energy, all compensated by $k^{3/2}$.

which measures the fraction of energy contributed at wavenumbers greater than or equal to k. Because the stresses are concentrated at the largest scales, this allows for a separation of scales and possibility of an inertial range, where the stresses are unimportant.

The field b_y plays the role of a background "guiding" field for the remaining small-scale fluctuations, whose energy spectrum is close to $k^{-3/2}$ in the interval $k \approx 4 - 20$. Indeed, this scaling is consistent with the inertial range of large-scale, driven, steady-state, MHD turbulence[3] (e.g., Maron and Goldreich, 2001; Haugen et al., 2004; Müller and Grappin, 2005; Mininni and Pouquet, 2007; Chen et al., 2011; Mason et al., 2006, 2008; Perez and Boldyrev, 2010b; Perez et al., 2012; Chandran et al., 2015). This was found in both the net-flux and zero-net-flux cases. The energy spectra are shown in Figs. 2.3, 2.7, and 2.8, for Cases I, II, and III, respectively. Cases I and

[3]In the studies of driven MHD turbulence (e.g., Perez et al., 2012), one typically uses the Reynolds number based on the velocity fluctuations. In our Case I, this would give $\mathrm{Re}_{\mathrm{rms}} = v_{\mathrm{rms}}(L_z/2\pi)/\nu \approx 4000$.

Table 2.2: Steady-state cases I, II, and III, and decaying case IV. The last two columns show best fits of the exponents of $E(k) - 0.5\, b_y^2(k) \propto k^{-\zeta_\perp}$ and $0.5\, b_y^2(k) \propto k^{-\zeta_\parallel}$ over the range $k \in [4, 20]$. For Case IV, the spectra are computed for $t/t_0 \in [20, 50]$.

Case	B_0	E	$\tilde{\alpha}$	ϵ/E	$\zeta_\perp$	$\zeta_\parallel$
I	0.030	0.71	0.37	0.52	1.50 ± 0.03	1.95 ± 0.02
II	0.010	0.41	0.22	0.54	1.51 ± 0.03	1.96 ± 0.03
III	0.005	0.072	0.039	0.54	1.13 ± 0.08	1.45 ± 0.12
IV	0.0	-	-	0.54	1.48 ± 0.04	1.95 ± 0.04

II are very similar, while Case III had much less energy and, therefore, no discernible inertial range. See Table 2.2. This suggests that the observed spectral behavior is independent of a net flux or of the overall level of turbulence, and that, instead, it is an inherent property of the shearing, rotating flow.

Further insight in the MRI-driven turbulence can be gained from Case IV,

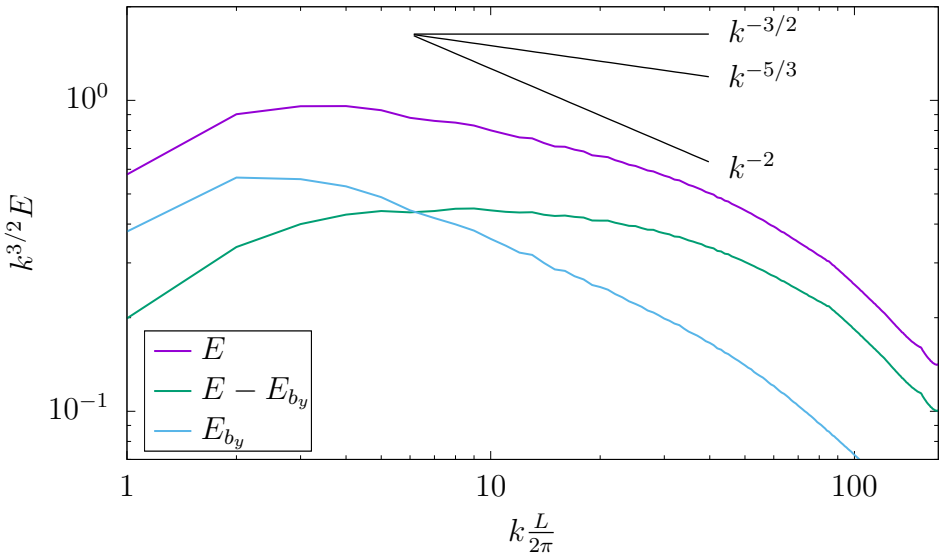

Figure 2.3: From Case I, energy spectra for the total energy, total without b_y, and b_y, all compensated by $k^{3/2}$.

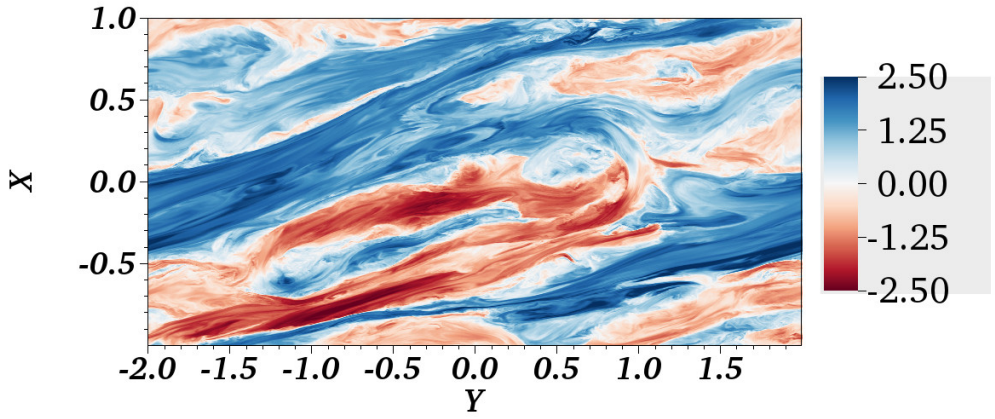

Figure 2.4: Snapshot during Case I of b_y, showing elongation of structures in y direction and regions of strong, counter-aligned b_y field.

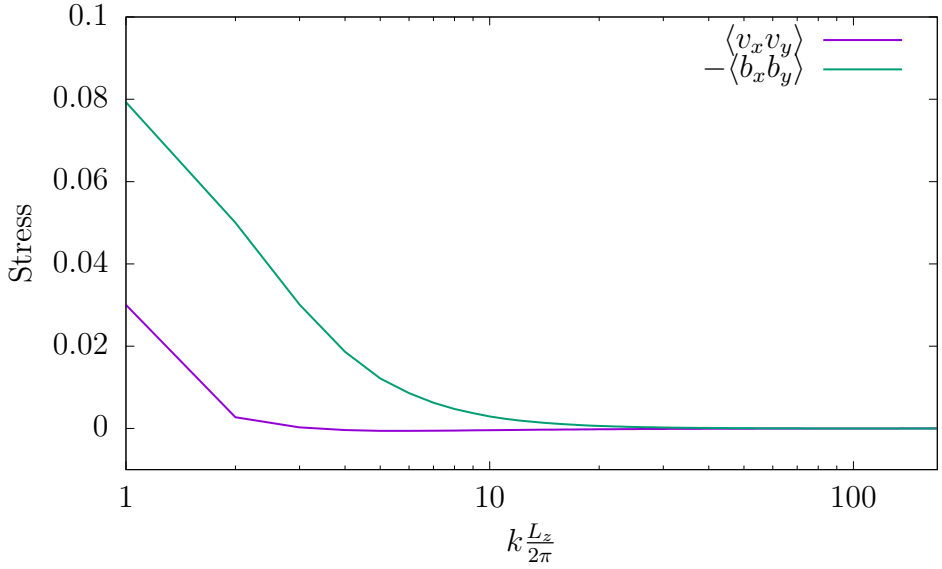

Figure 2.5: The Reynolds and Maxwell stresses at wavenumber k, from Case I.

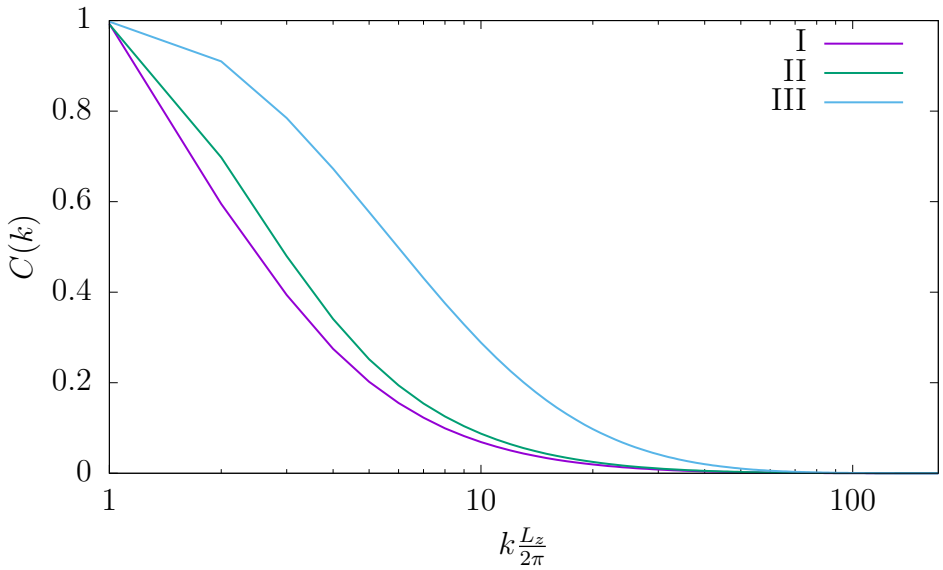

Figure 2.6: The cumulative energy injection rate at wavenumbers $\geq k$. Over 70% of the energy supplied comes from wavenumbers $k < 4$.

where no magnetic flux is imposed, and, in our case of Pm = 1, turbulence intensity declines, even if initiated at a high level. The decline is, however, very slow, on the order of $100t_0$; so the system is observed to go through a sequence of quasi-steady states. In these states, as seen in Fig. 2.1, the energy injection rate $\tilde{\alpha}$ nearly balances the rate of energy dissipation ϵ, and, therefore, the rate of energy cascade due to turbulence. The scaling of the turbulence energy spectrum does not noticeably change during this evolution, while both the turbulent energy E and the energy injection rate $\tilde{\alpha}$ slowly decay with time. An interesting property of such evolution is that the ratios ϵ/E and $\tilde{\alpha}/\epsilon$ remain nearly constant, as seen in Fig. 2.1 and in Table 2.2. This indicates that the energy cascade time at the outer scale of turbulence is the same for all the observed quasi-steady states.

A similar behavior is observed in the steady-state, MRI-driven cases, which we now analyze in greater detail. We compare the three steady-state cases I-III, whose parameters and results are summarized in Table 2.2.

Similarly to the decaying case, we observe that while energy, dissipation and injection rates all change with the the imposed flux, the ratios ϵ/E and $\tilde{\alpha}/\epsilon$ remain constant. For a quantitative analysis of this phenomenon, in Fig. 2.9 we plot the auto-correlation function of the fluctuations $R(x) = \langle \boldsymbol{v}(\boldsymbol{r} + x\hat{\boldsymbol{x}}) \cdot \boldsymbol{v}(\boldsymbol{r}) + \boldsymbol{b}(\boldsymbol{r} + x\hat{\boldsymbol{x}}) \cdot \boldsymbol{b}(\boldsymbol{r}) \rangle$. The width of the auto-correlation function gives the typical scale (i.e., the outer scale) of the fluctuations, while its amplitude $R_0 = \langle v^2 \rangle + \langle b^2 \rangle$[4] gives their typical strength.

We observe from the lower panel of Fig. 2.9 that the auto-correlation functions become remarkably similar if their spatial scales are renormalized by $R_0^{\varsigma_x}$. The best fit is given by $\varsigma_x \approx 0.43$, which is close to the value $\varsigma_x = 0.5$ expected for the constant non-linear interaction rate of large-scale turbulent fluctuations. Indeed, a simple phenomenological consideration estimates this rate as v_0/λ_0, where $v_0 = R_0^{1/2}$ is the intensity of fluctuations. A slight

[4] $\langle \cdot \rangle$ here and in the definition of $R(x)$ indicates a spatial average over each snapshot and an additional average over several snapshots.

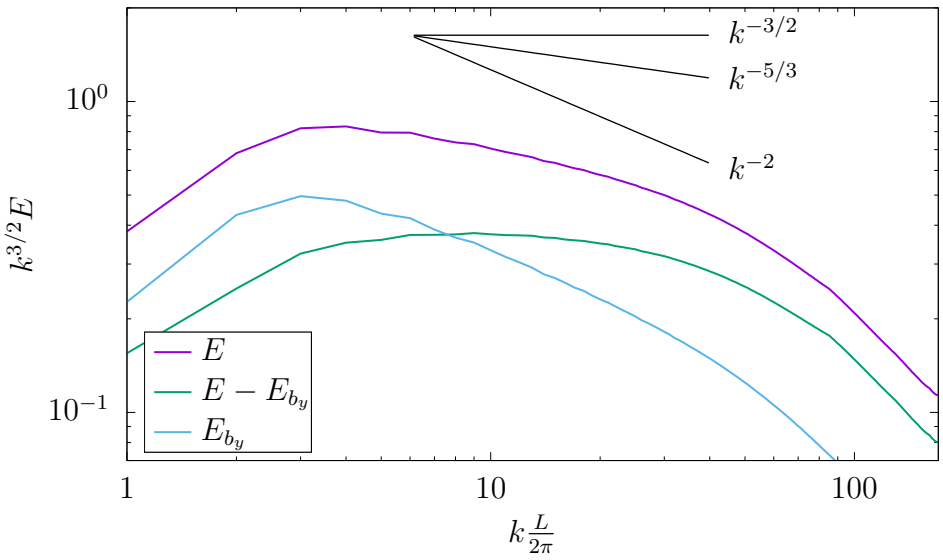

Figure 2.7: From Case II, energy spectra for the total energy, total without b_y, and b_y, all compensated by $k^{3/2}$.

discrepancy between the two scalings may be related to the limited Reynolds numbers currently available to our analysis. For larger Reynolds numbers, we expect the form of the renormalized correlation function to be largely independent of Reynolds number.

2.3 Phenomenology

We propose the following phenomenological explanation for this observation. Under the sole action of the orbital shear in equations (1.20, 1.21) the energy is supplied to the system and transferred in the direction of large wavenumbers. From Eq. 1.33, we see that the long time behavior is $k(t) \sim t$. Under the sole action of non-linear interaction the energy is removed from all the scales by a turbulent cascade, lowering the energy at the peak wavenumber. See Fig. 2.10. The rate of non-linear interaction increases with the wavenumber while the orbital-shear rate remains constant. Therefore, the

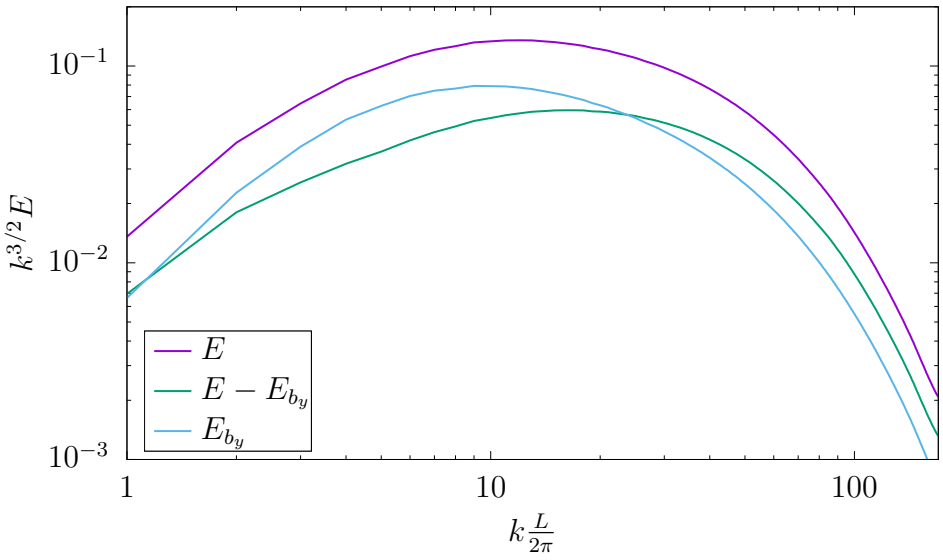

Figure 2.8: From Case III, energy spectra for the total energy, total without b_y, and b_y, all compensated by $k^{3/2}$.

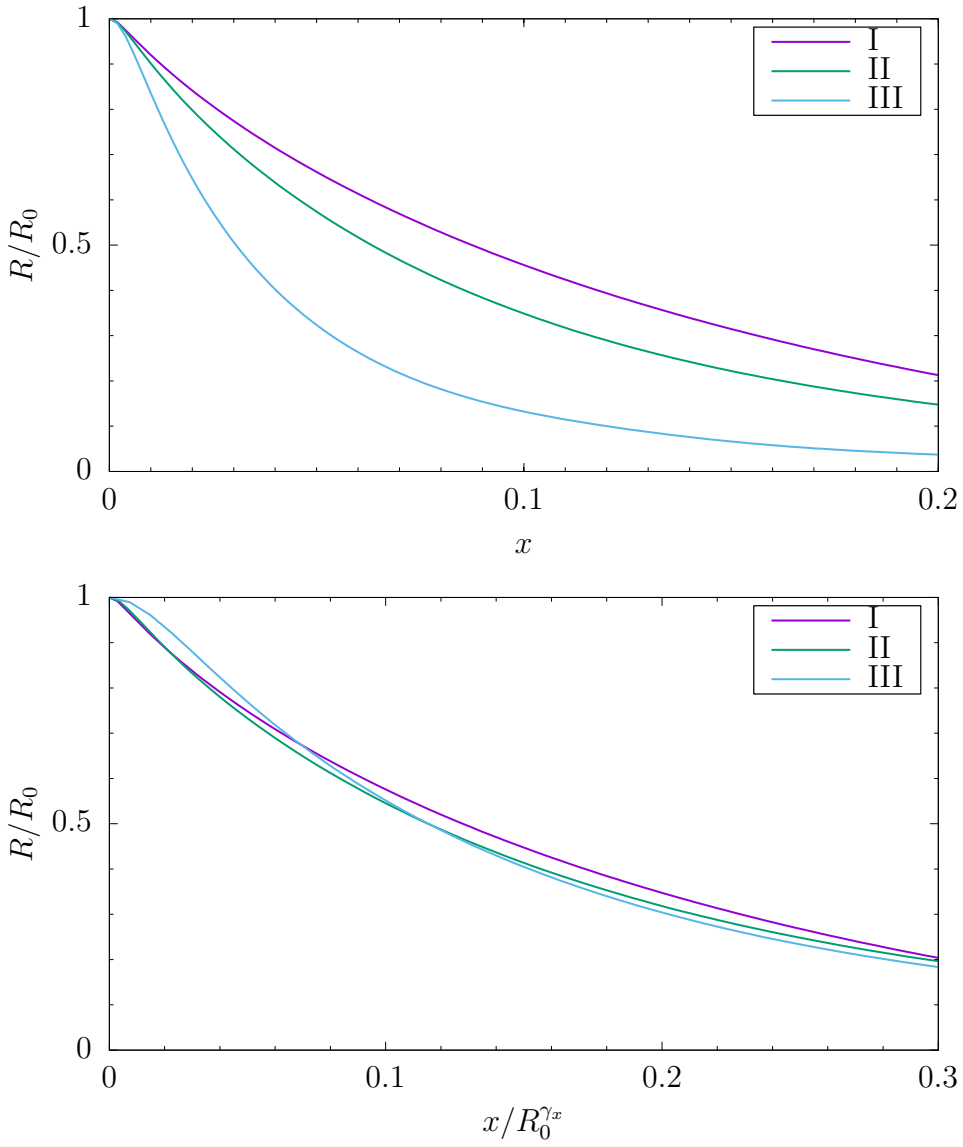

Figure 2.9: Upper panel: correlation functions for steady-state Cases I, II and III, each scaled to its respective maximum. Lower panel: the x-axis is rescaled by $R_0^{\varsigma_x}$, where $\varsigma_x \approx 0.43$ minimizes the distance between the curves.

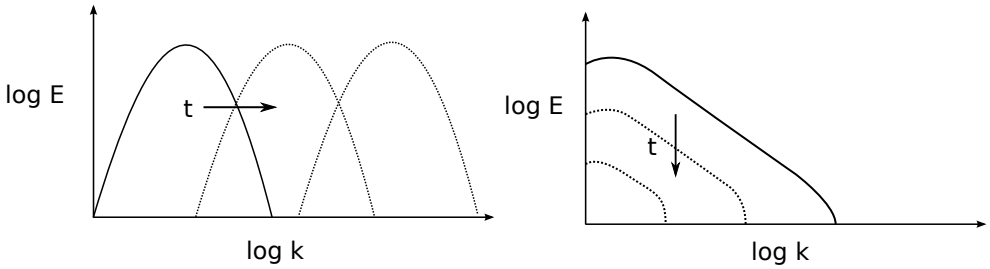

Figure 2.10: Left: Under the sole action of the shear, the energy spectrum is shifted toward higher wavenumbers. Right: Without constant energy injection, the turbulent cascade transfers energy to smaller scales where it is removed from the system by viscous and resistive dissipation.

orbital shear dominates at small k, while the non-linear interaction dominates at large k. At small wavenumbers where the orbital shear dominates, the energy is shifted in the phase space toward large k. This shift continues until the wavenumbers are reached where the rate of non-linear interaction competes with the orbital-shear rate and the energy is removed from large scales by a turbulent cascade. Therefore the scale λ_0 where the orbital shear is comparable to the rate of non-linear interaction,

$$\frac{v_0}{\lambda_0} \sim r\frac{\mathrm{d}\Omega}{\mathrm{d}r}, \tag{2.5}$$

becomes the outer scale of the resulting turbulence. See Fig. 2.11.

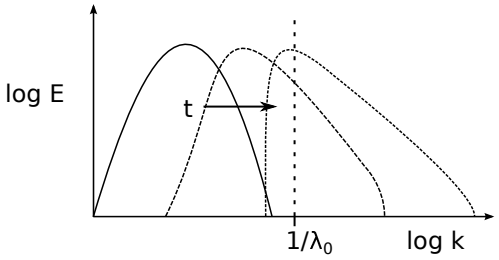

Figure 2.11: Linear shear and non-linear advection compete to set the outer scale λ_0 at the point where $S^{-1} \sim \lambda_0^{-1} v_0$, where the shear rate $S = -q\Omega_0 = r\frac{\mathrm{d}\Omega}{\mathrm{d}r}|_{\Omega=\Omega_0}$.

This condition constrains possible turbulent states in the shearing box. According to our consideration, the particular state may depend on the parameters of the system, such as the net magnetic flux. As we see in Table 2.2, however, all such states satisfy the constraint formulated above .[5]

2.4 Conclusions

The shearing-box model provides a simplified but highly nontrivial description of local turbulence in shearing, rotating flows. The mathematical properties of MRI-driven turbulence of such a "minimal" model are not fully understood. Although a rigorous mathematical description of shearing-box turbulence is not currently available, we have proposed a phenomenological picture of MRI-driven turbulence. We have shown that, first, the spectrum of MRI turbulence is independent of the mean field and may be understood in the framework of standard driven MHD turbulence Second, the outer scale of MRI turbulence adjusts so that the turnover time is a constant fraction of the large scale shear. We believe that these invariant features will be the founding principles of a future predictive model for MRI turbulence.

[5]It may seem that more detailed study of this phenomenology could be performed by varying the orbital shearing rate. We note, however, that varying the shearing rate *alone*, without changing other dimensionless parameters of the system, is a nontrivial task. Changing the shearing rate would imply changing the Rossby number (ratio of shear to rotation) which in turn would change the intensity of the resulting turbulence (e.g., Pessah and Chan, 2008).

3 MRI-DRIVEN TURBULENCE: ZERO NET FLUX

In this chapter, we concentrate on the case when the net magnetic flux through any cross-section of the box is zero. In this zero-net-flux case, a linear instability is not possible, but the flow may become unstable for a finite initial perturbation (subcritical instability) (Balbus and Hawley, 1992; Rincon et al., 2007; Lesur and Ogilvie, 2008; Herault et al., 2011; Riols et al., 2013; Squire and Bhattacharjee, 2014; Riols et al., 2016). It is not well understood under which conditions the turbulence within this system is self-sustained and driven by some reinforced subcritical instability, with different physical parameters (e.g. Pm) and simulation parameters (e.g. aspect ratio, viscosity) leading to different results (e.g., Lesur and Longaretti, 2007; Fromang and Papaloizou, 2007; Fromang et al., 2007; Nauman and Pessah, 2016).

Net-flux simulations we discussed in Chapter 2 concentrated on the case of unit magnetic Prandtl number and used a "short" shearing box ($L_z < L_x$), following the prescription of Bodo et al. (2008). A similar zero-net-flux setup was evolved for a long time (case IV in that chapter). We did not find dynamo action[1] for a magnetic Reynolds numbers several times larger than those required for the dynamo action in a non-shearing, non-rotating box. This observation cast doubt on the existence of MRI dynamo action for $\mathrm{Pm} \leq 1$, in a stark contrast with the non-shearing, non-rotating case where the dynamo action is expected to exist for any given Pm as long as the magnetic Reynolds number is large enough (e.g., Boldyrev and Cattaneo, 2004; Boldyrev et al., 2005; Iskakov et al., 2007; Malyshkin and Boldyrev, 2010). A different outcome of the shearing-box dynamo simulations was, however, reported in (Shi et al., 2016; Nauman and Pessah, 2016) who used the "tall" shearing boxes ($L_z > L_x$), that is, boxes that vertical sizes exceed

[1] We use the term "dynamo action" to refer to the self-sustained turbulence that results from the subcritical MRI instability that, in turn, reinforces the magnetic field.

the radial sizes. Quite interestingly, they observed that the critical Prandtl number for dynamo action is reduced as long as $L_z/L_x \gtrsim 2.5$.

In order to understand the different outcomes of these studies, we have performed a series of direct numerical simulations of incompressible MHD for varying aspect ratios of the zero-net-flux shearing box. We found that, in agreement with (Shi et al., 2016) and (Nauman and Pessah, 2016), the dynamo action is sensitive to the aspect ratio of the box. In our case of $\mathrm{Pm} = 1$, tall boxes rapidly exhibit dynamo action. To explain these results we propose that the turbulent eddies caused by the dynamo, efficiently fold the magnetic field lines in the radial (x) direction. As a consequence, in the short box the x-scale of the generated B_y component of the magnetic field is always comparable to the scale of the turbulent eddies. In contrast, in the tall box the flux of B_y can spread in the vertical direction over the distances exceeding the scales of the turbulent eddies, which are constrained by the short x dimension of the box. The vertical mixing of the B_y field is thus suppressed in tall boxes. As a result, different vertical sections of the tall box are permeated by large-scale nonzero fluxes of the azimuthal field B_y, leading to the instability.

The similarity and the universality of behavior of small scales in MRI turbulence and in driven MHD turbulence lend support to the suggestion in (Fromang et al., 2007) that the higher Rm-number threshold for the dynamo action observed in the low Pm-number, magnetorotational case may be related to the similar effect observed in driven, isotropic turbulence. Analytic consideration (e.g., Boldyrev and Cattaneo, 2004; Malyshkin and Boldyrev, 2010) and numerical simulations (e.g., Iskakov et al., 2007) suggest that the turbulent magnetic dynamo action has a higher-threshold magnetic Reynolds number in low-Prandtl-number systems. While in the case of magnetohydrodynamic turbulence the Rm-threshold value saturates as Pm decreases (e.g., Kraichnan and Nagarajan, 1967; Vainshtein and Kichatinov, 1986; Boldyrev and Cattaneo, 2004; Malyshkin and Boldyrev, 2010), it

remains to be seen whether a similar behavior holds in the magnetorotational case.

Early results from our simulation of turbulent system indicated that the MRI dynamo was nonexistent for $\mathrm{Rm} = 45\,000$. This Reynolds number is about 8 times larger than the critical Reynolds number required for the dynamo action at $\mathrm{Pm} = 4$ (Fromang et al., 2007). This indicates that the MRI dynamo action at $\mathrm{Pm} \leq 1$, if possible at all, is much more difficult to obtain than the magnetic dynamo action in isotropic, non-rotating turbulence, for which the threshold at $\mathrm{Pm} \ll 1$ is only about 3 times higher compared to the threshold at $\mathrm{Pm} > 1$ (Iskakov et al., 2007).

This phenomenological picture motivated us to review the results from our previous work (Walker et al., 2016, case IV). In that work, we simulated a short box with $(L_x, L_y, L_z) = (2, 4, 1)$ and $\mathrm{Rm} = 45\,000$. The initial large-scale fluctuations kept decaying for more than 200 shearing times. During this decay, the scale of the turbulence kept decreasing as well, as to maintain the balance between the linear and turbulent shear rates. For the large Reynolds number that we used, the turbulence would decay to progressively smaller scales. In this case, however, the scale of the turbulent fluctuations should eventually become sufficiently smaller than the vertical extent of the box L_z, so that according to our phenomenological picture, the dynamo should become possible. To check this hypothesis, we significantly extended the running time of simulations (Walker et al., 2016, case IV), and after about 600 shearing times did observe the possible onset of the dynamo action.

This may reconcile the available numerical results. Based on our findings, we suggest that the dynamo action is always possible, no matter what the aspect ratio of the box is. However, the short boxes require significantly larger Reynolds number and (assuming large scale of the initial fluctuations) significantly longer running time in order to observe the dynamo action. We have also established that the dynamo action leads to a quite intermittent

distribution of the azimuthal magnetic fluxes, in agreement with the proposed phenomenological picture.

3.1 Methodology

We will again solve the equations of the shearing-box model 1.20–1.23 and use numerical implementation of the SNOOPY code, as discussed in Section 1.5.

In our work, we consider three simulation boxes with the following dimensions $(L_x, L_y, L_z) \in \{(1,4,4),(1,4,16),(2,4,1)\}$. The numerical resolution in the first two cases is 128 points per unit length of L_x and L_z, and 64 points per unit length of L_y. In the third case, there are 512 points per unit length of L_x and L_z, and 256 points per unit length of L_y. Thus, the first and last cases have the same number of points in the vertical direction and are comparable after rescaling the unit of length. The first two cases have a viscosity of $\nu = 1/5000$. The third case has a viscosity of $\nu = 1/45000$. Cases I and II were initialized with $\boldsymbol{B}_0 = (0, 0, B_0 \cos(2\pi x/L_x))$ and a large-scale, white-noise velocity configuration, and then evolved until a steady state is reached. Case III is the continuation of the zero-net-flux simulations discussed in the previous chapter (case IV, there).

A summary of the cases studied is given in Table 3.1. Note that the energy and transport parameter reported are volume densities of these quantities. The turbulent transport parameter is defined as $\alpha = \langle v_x v_y - b_x b_y \rangle / (\Omega_0 L)^2$. Viscous transport is reported in the table as $\alpha_\nu = \frac{\nu S}{\Omega L}$. The values shown in the table are averages over some time intervals in the steady states (cases I, II, and IIIb), and over a short time interval in the decaying case IIIa, where the energy is approximately constant.

[2]These values are different than those reported in Walker and Boldyrev (2017) because of normalization. In that article, all values of stress were normalized by $\alpha = \langle v_x v_y - b_x b_y \rangle / (q\Omega_0 L_z)^2$. However, Cases I and II use the velocity unit $L_x\Omega$ instead of $L_z\Omega$. Thus a more appropriate normalization is $\alpha = \langle v_x v_y - b_x b_y \rangle / (\Omega_0 L_x)^2$ for Cases I

Case	$L_x \times L_y \times L_z$	ν^{-1}	E	$\alpha\ (\times 10^{-2})$	$\alpha_\nu\ (\times 10^{-2})$
I	$1 \times 4 \times 4$	5000	0.015	0.53	0.03
II	$1 \times 4 \times 16$	5000	0.15	4.7	0.03
IIIa ($t = 222$)	$2 \times 4 \times 1$	45000	0.017	0.28	$0.00\overline{3}$
IIIb ($t > 800$)	$2 \times 4 \times 1$	45000	0.0015	0.0037	$0.00\overline{3}$

Table 3.1: Setups examined in this study. The final case (III) is decaying until $t \approx 600$, and the numbers given for E and α are the values averaged over short time intervals around the indicated times.[2]

In the analysis presented below, one-dimensional energy spectra are computed from the three-dimensional Fourier components by summing over the other two dimensions. For example, for a field f, the energy spectrum $E(f)_{k_x}$ is computed as

$$E(f)_{k_x} = \frac{1}{2} \sum_{k_y,k_z} |f_{k_x,k_y,k_z}|^2, \tag{3.1}$$

giving the total energy in f for all modes with a specific k_x.

3.2 Results

Consistent with previous simulations (Nauman and Pessah, 2016), we find that our boxes with the aspect ratio $L_z/L_x \geq 4$ (cases I and II) are turbulent. They rapidly reach a steady state and maintain it for the extent of the simulation, while E and α fluctuate around a mean value. Case III, which is a continuation of (Walker et al., 2016, case IV), exhibits very slowly decaying turbulence until $t \approx 600$, and appears to reach a steady state at later times (see Fig. 3.1).

In an attempt to explain these results, we find it useful to study the behavior of the azimuthal magnetic field b_y. As was noted in Chapter 2, this field is concentrated at relatively large scales, and plays the role of the

and II and $\alpha = \langle v_x v_y - b_x b_y \rangle / (\Omega_0 L_z)^2$ for Case III, as adopted here.

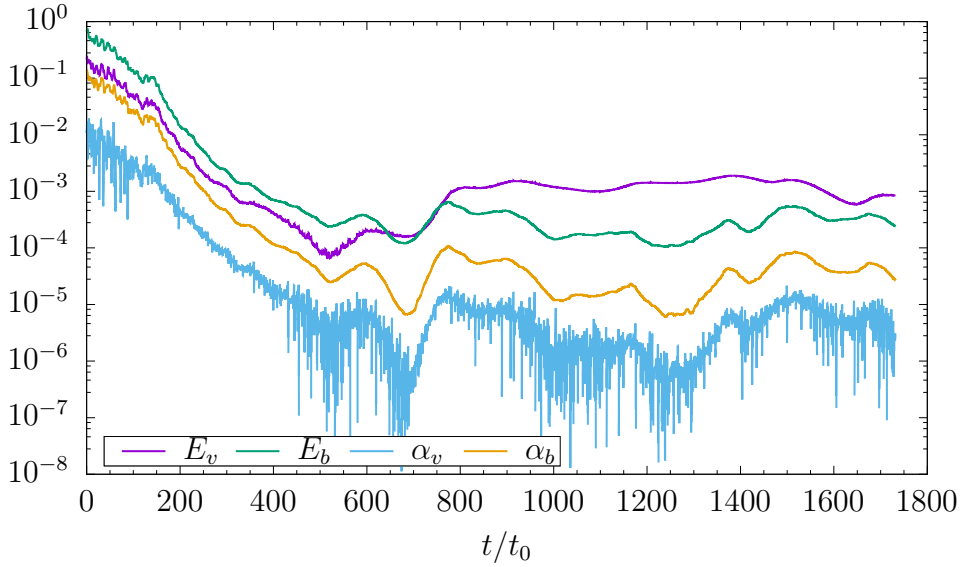

Figure 3.1: Time history for case III, showing the kinetic energy E_v, magnetic energy E_b, Reynolds stress $\alpha_v \equiv \langle v_x v_y \rangle / (\Omega_0 L_z)^2$, and Maxwell stress $\alpha_b \equiv \langle -b_x b_y \rangle / (\Omega_0 L_z)^2$.

guide field for the remaining fluctuations. We found, however, an important difference in the distribution of this field in tall and short boxes. The net flux of the b_y field is zero in the dynamo case. Given some significant initial perturbation of the magnetic field, the flow is subject to a sub-critical, transient growth, referred to as the "azimuthal MRI" (See Sec. 1.2). This leads to stretching and folding of the magnetic field lines in the x–y plane as the resulting flow distorts the magnetic field. The constant shearing flow then increases the strength of the b_y field. An important observation, however, is that the x-scale of the resulting folds of the b_y field is always on the x-scale of the fluctuating velocity field. In the box extended in the x-direction (case III), this means that both the b_y and the v_x fields are still concentrated at comparable scales. This is seen in the spectra shown in Fig. 3.2.

The situation is qualitatively different in a box extended in the vertical

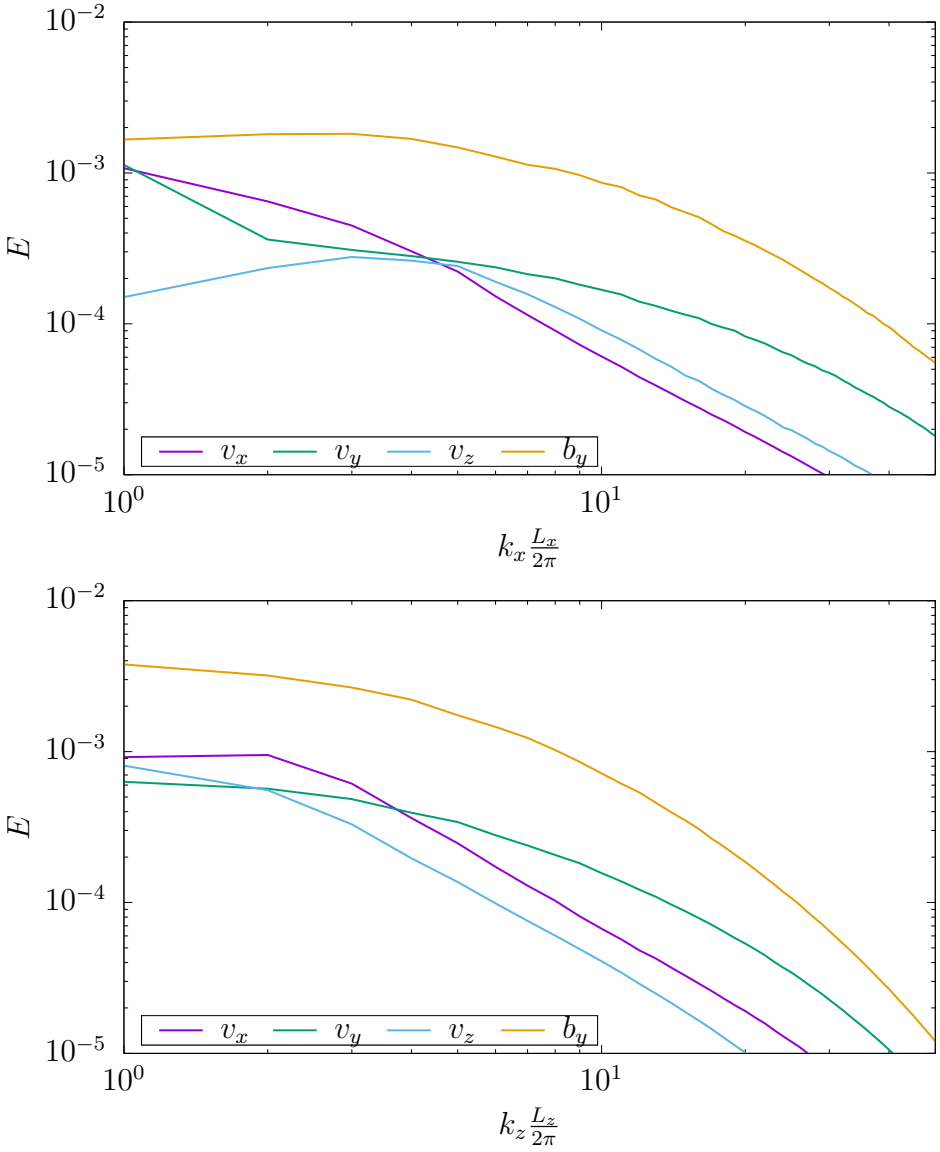

Figure 3.2: Energy spectra for case IIIa in the x-direction (upper panel) and z-direction (lower panel).

direction (case II). It turns out that in this case the flux of b_y can spread in the vertical direction over the scales much larger than the scales of the velocity field. This is seen in Fig. 3.3, where the v_z component of the velocity field is concentrated at the scale comparable to the small horizontal box size L_x, while the b_y magnetic field is concentrated at the larger scale L_z. The structure of the b_y field is shown in Fig. 3.4, which also reveals separation of the regions of positive and negative azimuthal magnetic flux in the vertical direction. This is in contrast to Fig. 3.5 where b_y is more homogeneous, due to large-scale turbulent mixing. Fig. 3.6 shows case I, an intermediate between cases II and III.

Levels of transport

In contrast to the relatively consistent values reported in the literature for the case with a net flux, transport within the zero-net-flux box vary considerably with the parameters of simulation used. For example, Shi et al. (2016) reported values of $\alpha \approx 0.002 - -0.2$. Here, we find that the taller boxes exhibit higher levels of transport, as can be seen in Table 3.1. From case I to case II, a quadrupling of the height of the box resulted in ten times the value of transport. In the case of our short box, the transport is only $\alpha = 3.7 \times 10^{-5}$ and, in fact, is comparable with the viscous stress $\alpha_\nu = \overline{3} \times 10^{-5}$. This indicates that for a system with solutions restricted more in the vertical direction than the radial direction ($L_x > L_z$) the turbulence transports no more angular momentum than viscous stresses. Disk models generally assume that turbulent stresses are orders of magnitude higher than viscous stresses. Possible conclusions are that either the disks cannot self-magnetize, since the magnetic fields generated are not enough to drive disk-creation, or the incompressible, periodic shearing box is missing key physics that lead to sustained turbulence with high levels of transport. Another explanation is that the Reynolds numbers are not high enough to distinguish between the outerscale and the viscous scale, that we have found

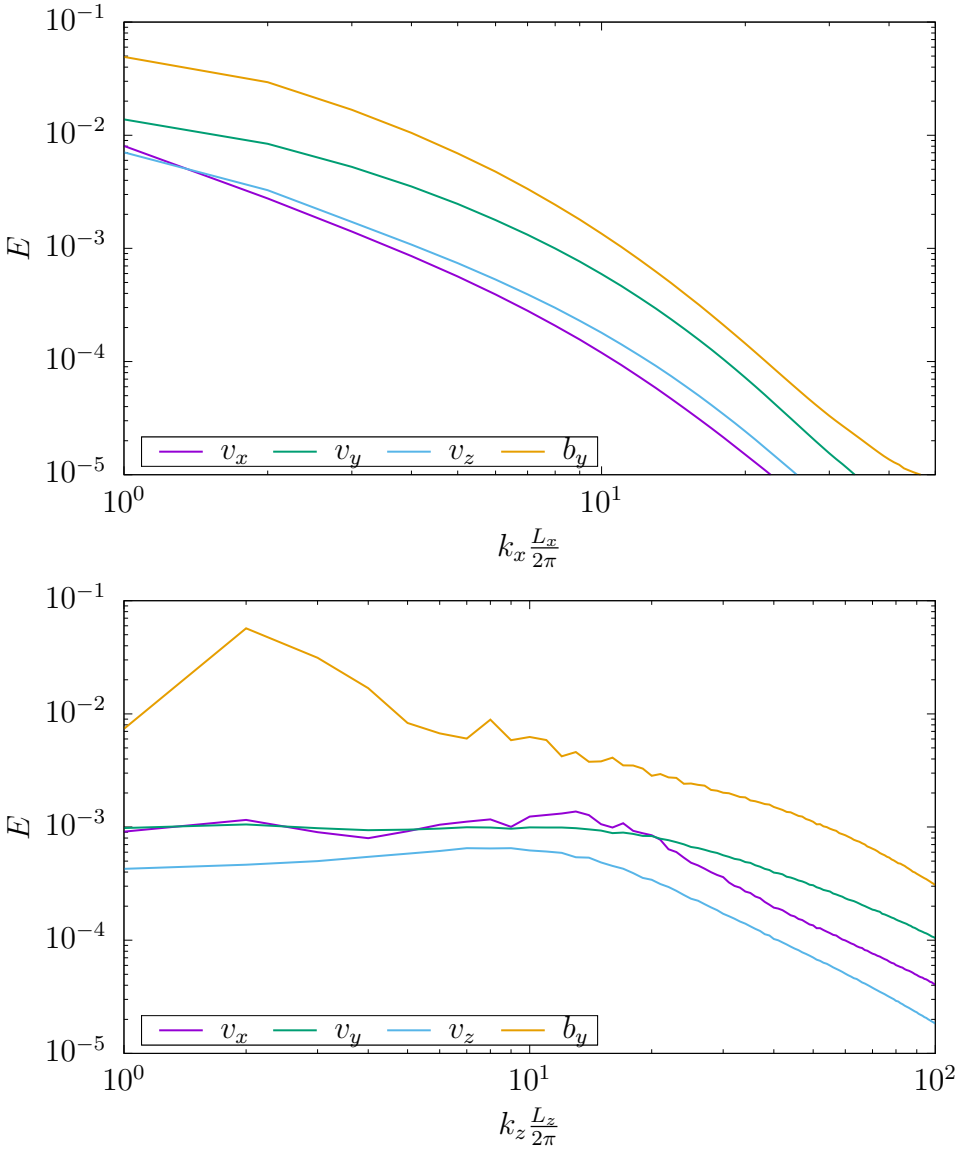

Figure 3.3: Energy spectra for case II in the x-direction (upper panel) and z-direction (lower panel).

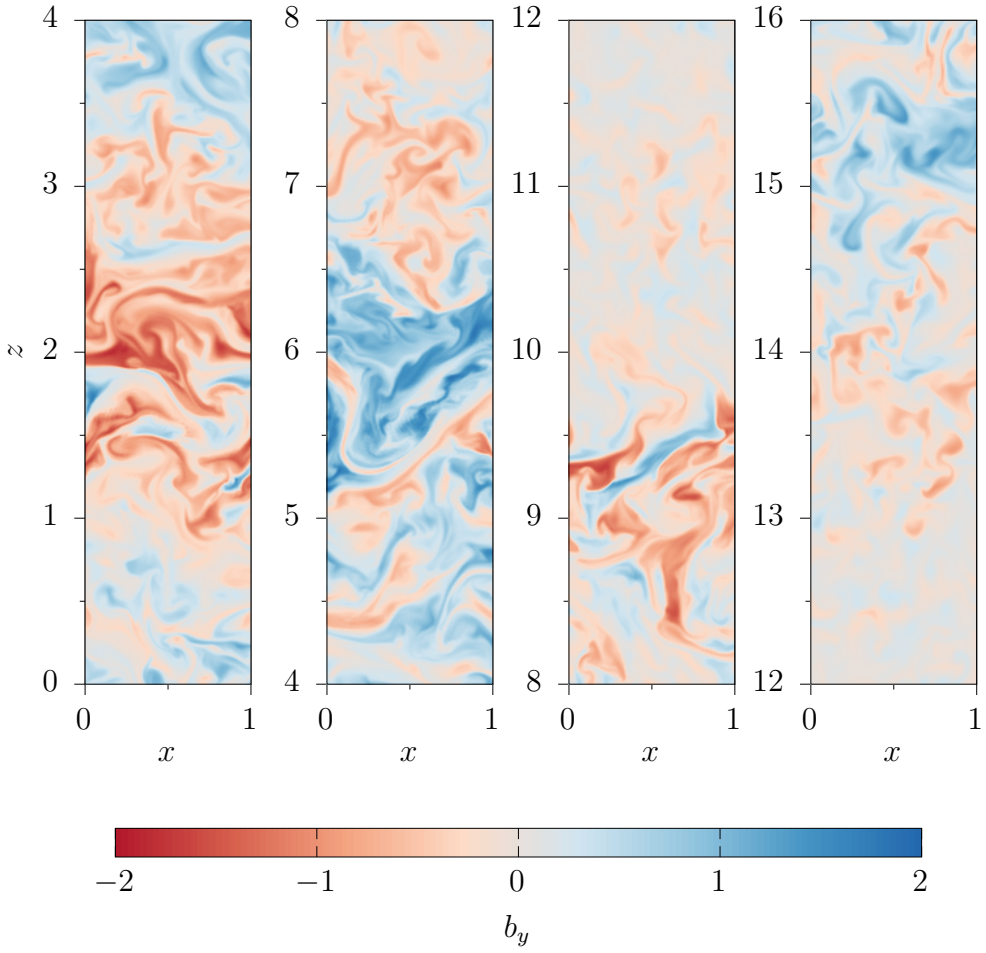

Figure 3.4: Snapshot of b_y from case II at a late time when a steady state has been reached. Note that domain extends from 0 to 16 in the z-direction, but it has been partitioned here for ease of viewing.

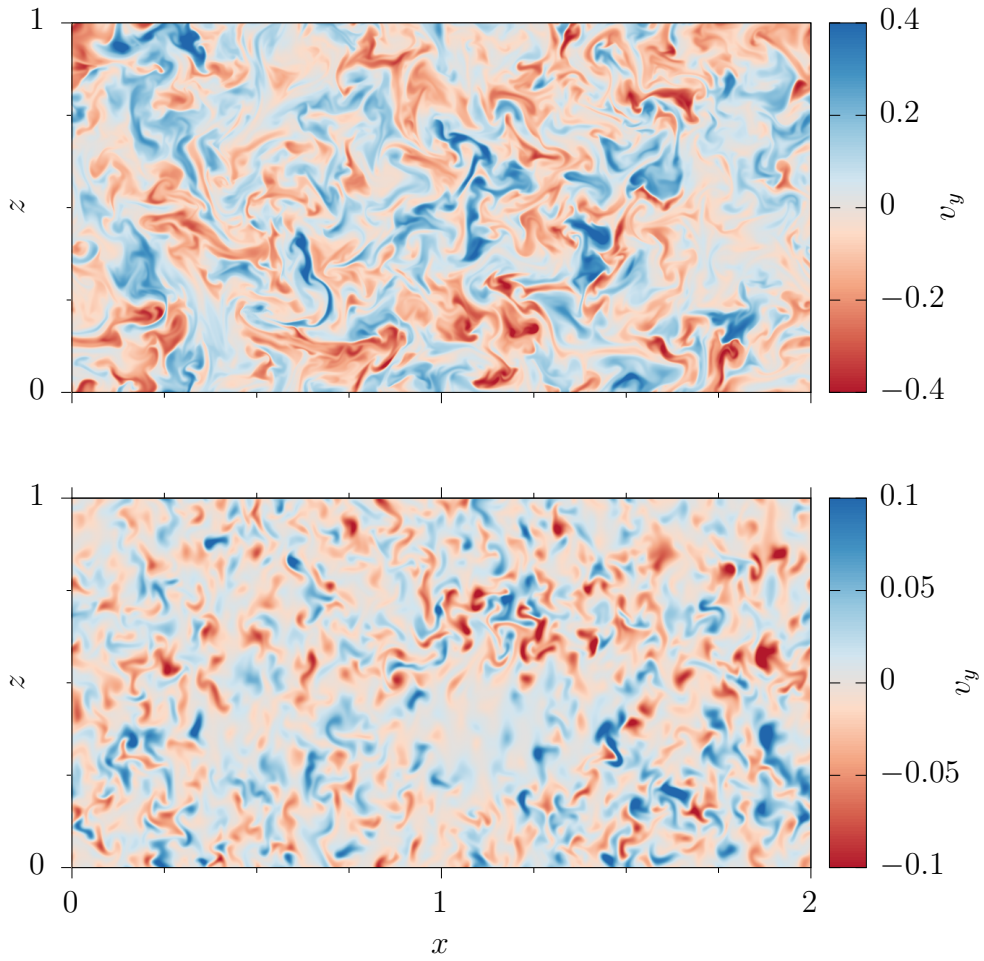

Figure 3.5: Snapshots of b_y from case IIIa ($t = 222$, top panel) and case IIIb ($t = 907$, bottom panel). Note the decreasing scale of structures between IIIa and IIIb.

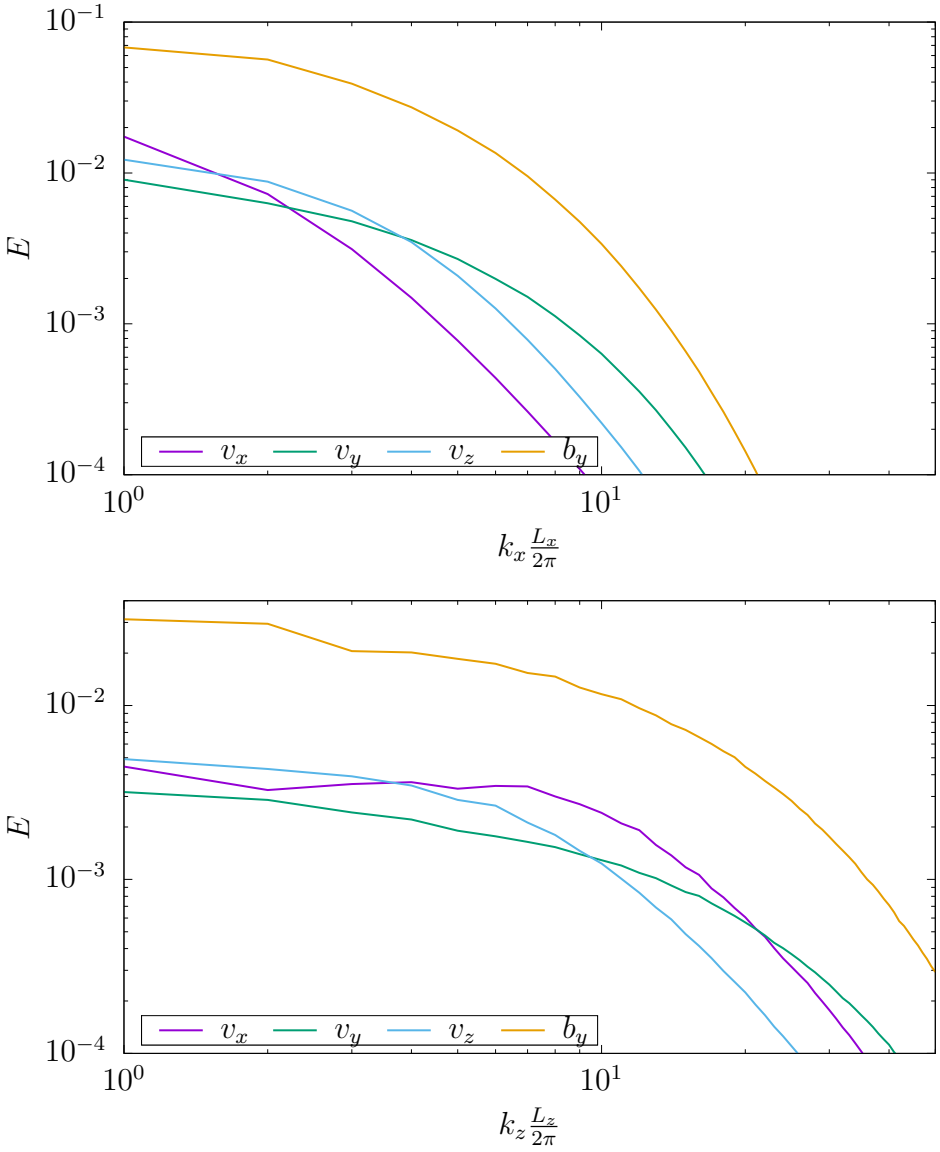

Figure 3.6: Energy spectra for case I in the x-direction (upper panel) and z-direction (lower panel).

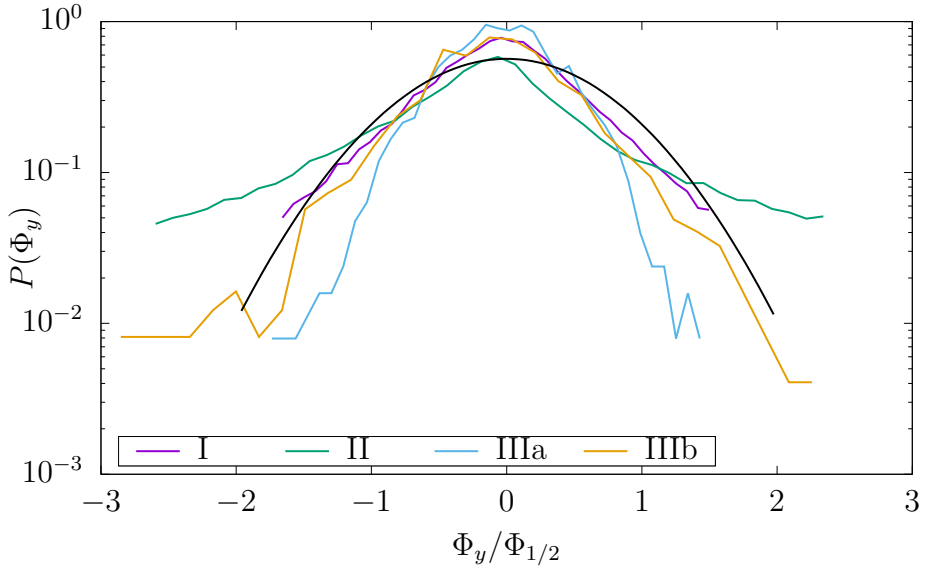

Figure 3.7: PDFs of flux Φ_y computed for each of the cases studied. Each data set has been rescaled by the full width at half maximum $\Phi_{1/2}$.

a marginal state. Because a turbulent disk that has zero net flux will have regions that contain a flux, this result demonstrates, at the very least, that the regions without a flux will contribute negligibly to the overall transport.

In order to quantify this flux intermittency and to compare it with the other cases, we subdivided $y = \text{const}$ cross-sections of the simulation boxes into small $1/16 \times 1/16$ squares and calculated azimuthal magnetic fluxes for each of these squares. We then plotted histograms of the obtained fluxes Φ_y. The results are shown in Fig. 3.7. The flux intermittency is smallest in case IIIa, larger in case I, and the largest in the tallest box of case II. The increased flux intermittency implies more favorable conditions for the dynamo action.

We are now in a position to answer why our case III did not exhibit dynamo action until the turbulence decayed to very small amplitudes (see Fig. 3.1). The matter is that when the energy of fluctuations declines, so does the scale of the turbulence (see Fig. 3.5, upper panel). In our work

(Walker et al., 2016) this is explained by the necessity to maintain the balance between the linear and nonlinear shearing rates of the turbulence. When the x-scale of the turbulence was relatively large compared to the box size L_z, the dynamo did not operate strongly enough to self-sustain turbulence. When the x-scale of the turbulence decreased to become smaller than the L_z size of the box, in analogy with cases II and I, the dynamo action became possible. Consistent with our discussion above, the intermittency of the magnetic flux also increased in this regime (see Fig. 3.7).

Although the dynamo action seems to operate in case IIIb, we should exercise caution in claiming that a true steady state is observed. As pointed out in (Rempel et al., 2010) it may be possible in such a case that the system is described by a super-transient state and may ultimately decay if integrated long enough[3]. Also, unlike the other dynamo cases in this study, IIIb has developed, in addition to the small-scale fluctuations, a large-scale $v_y(x)$ zonal flow resulting from geostrophic balance (Johansen et al., 2009) (see Fig. 3.8). Comparing the spectra of case III from early times in Fig. 3.2 with those from late times in Fig. 3.9, we see that this zonal flow is long-lived, or at least steadily reinforced. The possibility of such a flow may be related to the long radial extent of the box. This flow, however, is practically uncorrelated with the small-scale fluctuations; for instance, it does not contribute to the transport coefficient α_v in Fig. (3.1).

3.3 Conclusions

We have found in incompressible MHD simulations of the shearing box that the properties of the zero-net-flux dynamo action depend intimately on the relation between the scale of the turbulence and the vertical aspect ratio of the box. For a given set of physical parameters, transport is sustained and dynamo action rapidly sets in in systems with high L_z/L_x aspect ratio, while

[3] Although, with $\mathrm{Rm} = 45000$, the expected lifetime is $\mathcal{O}(10^{32}\Omega)$.

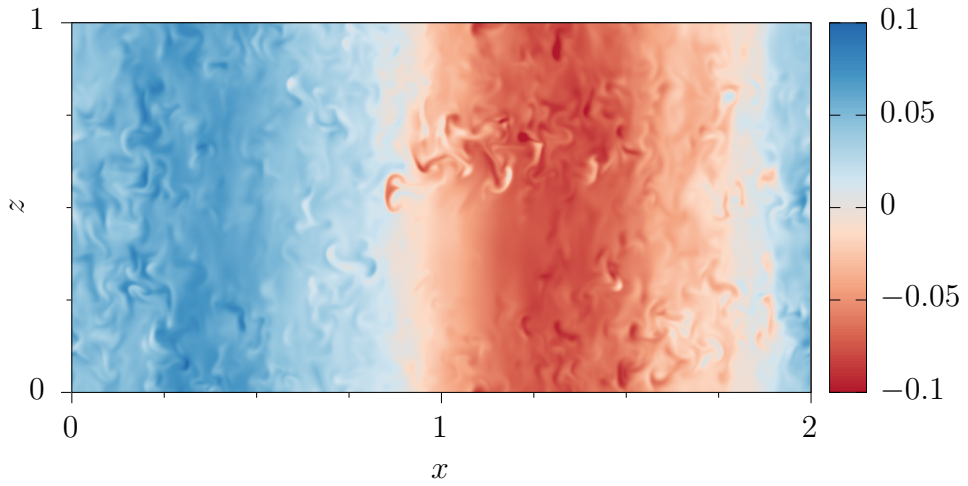

Figure 3.8: Snapshot of v_y from case IIIb.

in the opposite case of small aspect ratio, dynamo action is not observed until the scale of the turbulence significantly decreases. This is the despite the size of the box being much greater than the dissipative scale of turbulence in both cases.

Based on our results we suggest the following explanation for this phenomenon. We propose that an inherent property of the shearing-box turbulence is its tendency to build up local regions of nonzero b_y flux, separated in the vertical direction z. This may be related to the fact that the configurations $\boldsymbol{b} = (0, b_y(z), 0)$, $\boldsymbol{v} = (v_x(z,t), v_y(z,t), 0)$ are exact solutions of the ideal equations (e.g., Goodman and Xu, 1994). Those sub-regions with nonzero b_y fluxes are MRI-unstable. The resulting turbulent eddies, on the other hand, are trying to mix and homogenize the b_y field. The size of the turbulent eddies is always comparable to the size of the folds of the b_y field in the x-direction. Indeed, such eddies are caused by the MRI instability of the b_y field. In "short" boxes, the eddies caused by an initially unstable large-scale perturbation have a typical length-scale larger than the vertical

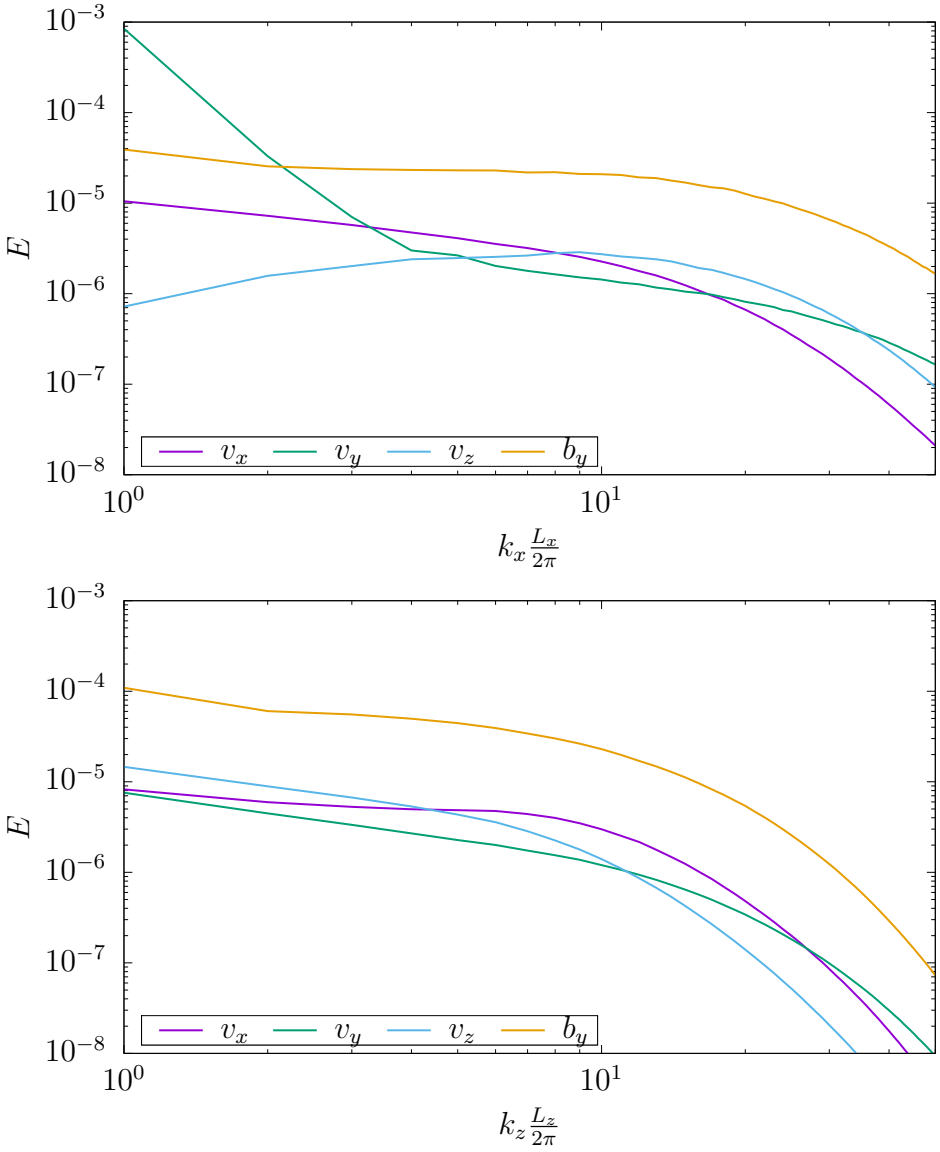

Figure 3.9: Energy spectra for case IIIb in the x-direction (upper panel) and z-direction (lower panel).

extent of the box, and they are able to effectively mix the field in that direction, thus reducing the b_y fluxes and effectively reducing the rate of the instability as compared to the rate of turbulent energy dissipation. The resulting turbulence will therefore decay, until the scale of the turbulence becomes smaller than the vertical size of the box, at which point the vertical flux separation enhances the efficiency of the instability. In "tall" boxes, on the other hand, the eddies are always smaller than the vertical extension of the box. This allows oppositely-directed b_y fluxes to build up in vertically separated regions, allowing the instability to win.

This poses a broader question to what extent the shearing-box results describe the natural MRI turbulence. The shearing-box model suggests that the scale of the MRI-dynamo-driven turbulence should be smaller than the thickness of the disc and that the resulting transport coefficients are very small. We, however, notice that the vertical limitations in real accretion disks are never as severe as the periodic boundary conditions of the shearing-box simulations. Allowing the flux of the b_y magnetic field to partially escape the box in the vertical direction, for instance, will facilitate the dynamo action rather than impede it. This indicates that the shearing-box model with periodic boundary conditions may not allow one, at least at the present level of understanding, to realistically simulate the scale and the transport properties of the MRI-dynamo-driven turbulence at low magnetic Prandtl numbers. What seems to be a robust feature of the MRI-dynamo-driven turbulence, however, is its tendency to separate the regions of positive and negative b_y fluxes, leading to highly intermittent azimuthal magnetic flux patches. In a stratified disk, these magnetic flux tubes can then buoy above the surface, forming an intermittently magnetized corona (e.g. Galeev et al., 1979). Non-periodic large-scale conditions (e.g., stratification, flux escape, etc.) need to be incorporated in the shearing-box model in order to provide a more realistic description.

4 INFLUENCE OF TEARING INSTABILITY ON MAGNETOHYDRODYNAMIC TURBULENCE

In the previous chapters, we were focused on turbulence driven by a constant shear and instability at the outer scale. In this chapter, we will be interested in the effect of magnetic shear and instabilities generated by the turbulent cascade itself.

As discussed in Sec. 1.3, the dynamic-alignment theory of MHD turbulence predicts as the scale decreases, increasingly anisotropic eddies are produced. Alfvénic eddies become progressively more ribbon-like at smaller scales, assuming the shape of current sheets. Given a very large Lundquist number, the ribbon-like eddies in the inertial interval of MHD turbulence may become affected by the tearing instability.

Carbone et al. (1990) first addressed this question in the framework of the Iroshnikov-Kraichnan (IK) model of MHD turbulence (Iroshnikov, 1963; Kraichnan, 1965). The tearing mode considered in Carbone et al. (1990) was essentially isotropic, which fit an assumption of the IK model[1]that MHD turbulence consists of isotropic (characterized by a single size) weakly interacting Alfvén waves at each scale. Moreover, the tearing mode considered in Carbone et al. (1990) required the presence of a significant velocity shear tuned to the magnitude and scale of the magnetic field (Hoffman, 1975; Dobrowolny et al., 1983; Einaudi and Rubini, 1986). The growth rate of this mode depended on the velocity shear, and it reduced to the standard Furth-Killeen-Rosenbluth (FKR) result Furth et al. (1963) as the velocity shear decreased Einaudi and Rubini (1986).

Loureiro et al. (2007) considered, instead, highly anisotropic current sheets of the kind found in models of reconnection. Apparently, these current

[1]The IK model has since been demonstrated to be incorrect, since weak MHD turbulence has the energy spectrum -2, not $-3/2$ proposed in the IK model (e.g., Ng and Bhattacharjee, 1996; Goldreich and Sridhar, 1997; Galtier et al., 2000).

sheets are unstable to a tearing instability with a maximum growth rate that scales as $\gamma \sim S^{1/4}$. An important consideration is that MHD turbulence, as described by DA theory and observed numerically, will naturally produce such anisotropic, current-sheet-like structures. The tearing rate of these structures grows with the anisotropy and can eventually be comparable to the eddy turnover time. Loureiro and Boldyrev (2017) and Mallet et al. (2017a) proposed that MHD turbulence should rather be modified at small scales by highly anisotropic tearing modes, which are beyond the FKR regime.

It was estimated that such a regime becomes relevant if the Lundquist number of turbulence becomes very large $S \gtrsim 10^6$ (e.g., Boldyrev and Loureiro, 2017).[2] Due to this severe computational constraint, direct numerical evidence in support of the tearing-mediated turbulence regime does not exist. It has been observed previously that the tearing instability initiated in a thin laminar current layer eventually leads to a broad range of non-linearly interacting and seemingly turbulent fluctuations (Huang and Bhattacharjee, 2016; Hu et al., 2018). In those works, however, the reconnection layer did not possess Alfvénic turbulence.

In this chapter, we present a method for studying anisotropic MHD turbulence in the tearing-mediated interval with a two-dimensional setup that models the transverse dynamics of a current sheet. Our method is somewhat analogous to the reduced-MHD (RMHD) approach in simulations of MHD turbulence (e.g., Kadomtsev and Pogutse, 1974; Strauss, 1976; Biskamp, 2003; Tobias et al., 2013). The RMHD equations apply when the simulation domain (a rectangular box) is permeated by a strong background magnetic field B_0, say in the z-direction. Assume that the rms values of magnetic and velocity fluctuations are normalized to unity, $v_{\rm rms} \sim b_{\rm rms} \sim 1$.

[2] We assume that at the outer scale the magnetic fluctuations are comparable to the velocity fluctuations and to the background magnetic field. We also assume that the fluid viscosity and magnetic diffusivity are on the same order, so the Lundquist, Reynolds, and magnetic Reynolds numbers are on the same order as well.

For the turbulence to be critically balanced at the largest scale, one needs to elongate the box in the z-direction proportionally to the value of B_0. In the case $B_0 \gg b_{\rm rms}$, the fluctuations of the z-components of the magnetic and velocity fields can then be neglected, and the MHD system is approximated by the reduced-MHD equations (see also (Oughton et al., 2017; Zhdankin et al., 2017)).

The novelty of our approach is that instead of studying turbulence driven at large scales, we study the evolution of a *particular highly anisotropic eddy* that is expected to exist at scales much smaller than the outer scale of the turbulence. For that we stretch the box in the x-direction as compared to the y-direction, $L_x \gg L_y$. For the eddy to be critically balanced, we need the following conditions at the box scale: $L_z/B_0 \sim L_x/b_x \sim L_y/b_y$, where $b_x \sim v_x$ and $b_y \sim v_y$ are typical fields in the x and y directions. The box-sized eddies in such turbulence are effectively very anisotropic current sheets. It is important to note that such eddies cannot be in a steady state; they are destroyed by nonlinear interaction on their Alfvénic time scale $\tau_A \sim L_x/b_x$. During their lifetime, however, they tend to develop small-scale turbulence inside them that, for a sufficiently large Reynolds number, should resemble regular, although very anisotropic, MHD turbulence.

If we increase the resistivity, however, the large-scale magnetic fluctuations will become subject to tearing instability (e.g., Furth et al., 1963; Coppi et al., 1976; Loureiro et al., 2007). The analysis of (Boldyrev and Loureiro, 2017) shows that the fastest-growing tearing mode in such an eddy has the growth rate $\gamma_t \sim (b_x/L_y)S^{-3/7}$, where the *local, eddy-scale* Lundquist number is defined as $S = b_x L_y/\eta$ and the magnetic field is measured in Alfvénic units.[3] In order for the tearing rate to become comparable to the eddy turnover rate $\gamma \sim 1/\tau_A \sim b_x/L_x$, we need to require $S = S_{\rm c} \sim (L_x/L_y)^{7/3}$. Therefore, if we need to perform computations with a large Lundquist

[3]Here we use the fact that the reconnecting magnetic field in our numerical setup has a sine profile. For a tanh-profile, the exponent 3/7 should be replaced by 1/2, which does not qualitatively change the results.

number S, we have to choose a very anisotropic box.

On the other hand, in order to reliably measure the scaling properties of the turbulence, the Reynolds number should be large. The *local* Reynolds number measuring the strength of the nonlinear interaction is defined as $\mathrm{Re} = b_y L_y/\eta$. It is smaller than the Lundquist number. For critically balanced fluctuations $b_y \sim b_x(L_y/L_x)$, the Reynolds number corresponding to S_c would thus be $\mathrm{Re}_\mathrm{c} \sim (b_y/b_x)S_\mathrm{c} \sim (L_x/L_y)^{4/3}$. The Alfvénic evolution time τ_A of such an eddy increases with the box elongation. If we assume that in order to resolve the inertial interval we need at least $\mathrm{Re} \sim 2000$, and $N_y = 512$ grid points in the shortest, L_y direction (see, e.g., (Perez et al., 2012)), we encounter prohibitively strong limitations for the numerical simulations, in both the number of grid points and the running time.

In an attempt to overcome these limitations, we use a simplified, two-dimensional setup. Although two-dimensional MHD is different from its three-dimensional counterpart, there are certain similarities between strong turbulence in the two cases. As observed numerically (e.g., Politano et al., 1998; Biskamp and Schwarz, 2001; Ng and Bhattacharjee, 2007; Wan et al., 2013), two-dimensional turbulence tends to form sheet-like magnetic structures at small scales, and its energy spectrum is close to $-3/2$, similar to the three-dimensional case. The eddy turnover rate should therefore scale in the same way as in three-dimensional turbulence. We believe that this should suffice for our study of the interplay of tearing and Alfvénic dynamics, at least on a qualitative level.

4.1 Methodology

We solve the incompressible MHD equations in a two-dimensional anisotropic periodic box with the pseudospectral code SNOOPY Lesur and Longaretti

(2007). The equations are

$$\partial_t \boldsymbol{v} = -(\boldsymbol{v}\cdot\boldsymbol{\nabla})\boldsymbol{v} - \boldsymbol{\nabla}P + \boldsymbol{B}\cdot\boldsymbol{\nabla}\boldsymbol{B} + \nu\nabla^2\boldsymbol{v} + \boldsymbol{f}, \tag{4.1}$$

$$\partial_t \boldsymbol{B} = \boldsymbol{\nabla}\times(\boldsymbol{v}\times\boldsymbol{B}) + \eta\nabla^2\boldsymbol{B}, \tag{4.2}$$

where $\boldsymbol{v}(x,y,t)$ is the velocity field, $\boldsymbol{B}(x,y,t) = b_0\sin(2\pi y+\phi)\hat{\boldsymbol{x}} + \boldsymbol{b}(x,y,t)$ is the magnetic field, P is the pressure, and $\boldsymbol{f}(x,y,t)$ is the external force. The magnetic field is measured in Alfvénic units. The large-scale magnetic field $b_0\sin(2\pi y+\phi)\hat{\boldsymbol{x}}$ is not an exact solution of the resistive MHD equations, therefore the $k_yL_y/(2\pi) = \pm1$ components of the magnetic field can change in time. We, however, update these particular components at each time step to ensure that the amplitude b_0 does not change. While this could be achieved self-consistently through forcing these modes with dynamically-tuned amplitudes, we find that our ad hoc method is very simple and effective. For simplicity, we choose $\mathrm{Pm} = \nu/\eta = 1$. We normalize the variables in such a way that $L_y = 1$, and $b_0 \approx 1$. The time is measured in units of L_y/b_0.

Currently, the exact dynamics of current sheet formation in MHD turbulence is not well understood.[4] The fluctuations inside our anisotropic eddy, therefore, are excited from zero level by an eddy-scale driving force. The amplitude of the anisotropic, solenoidal random force $\boldsymbol{f}(x,y,t)$ is chosen to ensure $v_x \sim v_{\mathrm{rms}} \lesssim b_0$; the box anisotropy requires $f_y \sim f_x(L_y/L_x)$. The force is applied in Fourier space. We force the modes $k_xL_x/(2\pi) = \pm1, \pm2$, $k_yL_y/(2\pi) = \pm1, \pm2$, with amplitudes drawn from a normal distribution and refreshed independently on average every $\tau_f \sim 1$ (a time short compared to the Alfvénic time of the eddy).

We simulate a strongly anisotropic eddy with dimensions $L_x \times L_y = 64\times1$. Note that in isotropically driven MHD turbulence, such structures are expected to exists at scales approximately 10^7 times smaller than the outer

[4] A mechanism of selective decay, related to the cross-helicity conservation may however be at play (e.g., Tobias et al., 2013).

scale of turbulence. We choose the numerical resolution of $N_x \times N_y = 32768 \times 512$ grid points. As discussed above, in order for the tearing-instability rate to match the eddy-turnover rate, the *local* Lundquist number, defined as $S = b_0 L_y/\eta$, should satisfy $S \sim (L_x/L_y)^{7/3} \sim 14000$, while for $S \gg 14000$, the turbulence is expected to resemble standard MHD turbulence (Boldyrev and Loureiro, 2017).

4.2 Results

We performed three simulations which differ only in the value of the Lundquist number: $S = 64000$, 16000, and 4000. It is important to note that if tearing were irrelevant the Lundquist number would not affect the time it takes to disrupt the eddy.

Consider, first, the case of the largest Lundquist number $S = 64000$. As seen in Fig. 4.1 (first panel), the anisotropic eddy is gradually destroyed by growing fluctuations of the b_y and v_y fields. The growth is slow, with a time scale comparable to the Alfvénic time scale, $\tau_{\rm A} \sim 64$. This time is shorter than the tearing time estimated as $\tau_t \sim (L_y/b_0)S^{3/7} \sim 115$. It is, therefore, expected that the tearing effects are not important, and indeed the spectrum of the turbulence developing inside the eddy during the eddy evolution is more consistent with that observed in Alfvénic turbulence ($-3/2$) (e.g., Maron and Goldreich, 2001; Haugen et al., 2004; Müller and Grappin, 2005; Mininni and Pouquet, 2007; Chen et al., 2011; Mason et al., 2006, 2008; Perez and Boldyrev, 2010b; Perez et al., 2012; Chandran et al., 2015; Perez et al., 2014a) than with the prediction for the tearing-dominated turbulence ($-19/9$), as is shown in Fig. 4.2. Typical current structures in this case are shown in Fig. 4.3. Plasmoid-like structures are not very common. Even when they appear, they do not have a chance to survive or grow to large scales. This is consistent with the expectation that the shearing flows associated with Alfvénic fluctuations tend to impede the tearing activity.

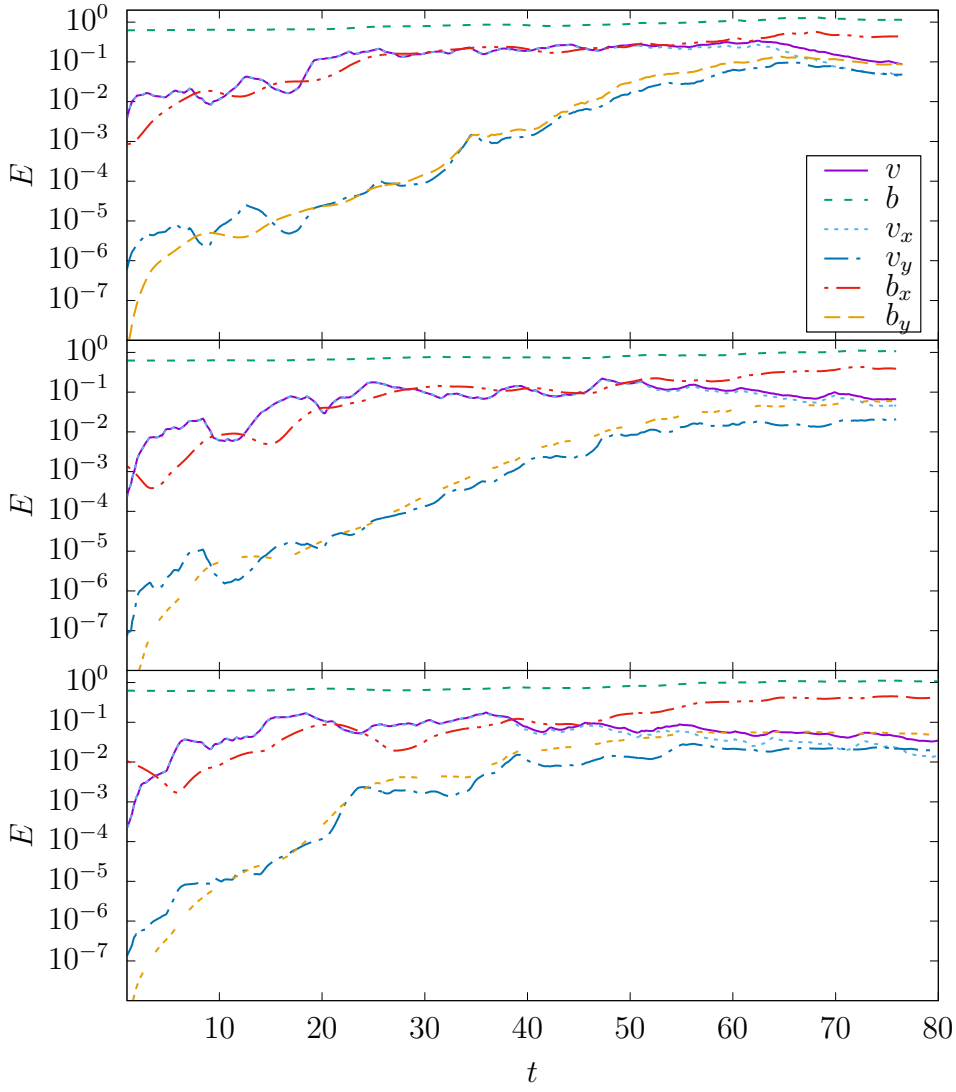

Figure 4.1: Time history of energy components. Top panel: $S = 64000$, middle: $S = 16000$, bottom: $S = 4000$. The fluctuating v_y and b_y fields are initially generated by the driving force at the level corresponding to 1/64 of their x-components. They grow due to nonlinear energy redistribution and/or tearing instability until they reach the magnitude of the x-components, at which point the anisotropic eddy is destroyed.

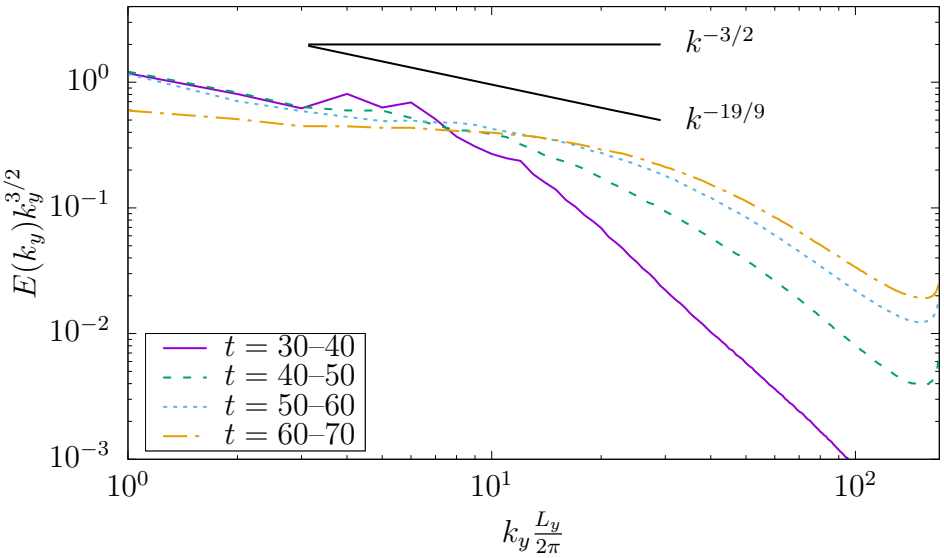

Figure 4.2: Compensated energy spectrum for the setup with $S = 64000$, shown at several instances of the eddy evolution. At the latest time interval the eddy has been destroyed by the nonlinear interaction. The spectrum at this stage is close to the spectrum of steady-state Alfvénic MHD turbulence.

The scaling of the alignment angle between the magnetic and velocity fluctuations, defined as

$$\theta_\lambda = \sin^{-1}\left(\frac{\langle \delta \boldsymbol{v}_\lambda \times \delta \boldsymbol{b}_\lambda \rangle}{\langle |\delta v_\lambda||\delta b_\lambda| \rangle}\right) \tag{4.3}$$

(see, e.g., (Mason et al., 2008) for more details), is also broadly consistent with MHD turbulence, even though its overall magnitude changes during the eddy evolution, as shown in Fig. 4.4.

The case of $S = 4000$ is shown in the bottom panel of Fig. 4.1. The Lundquist number is small enough so that the tearing time, $\tau_t \sim 35$, is shorter than the Alfvénic time. Therefore, we would expect the eddy to be disrupted faster than in the top panel ($S = 64000$), due to the action of the tearing instability. This observation is consistent with the conjecture (and

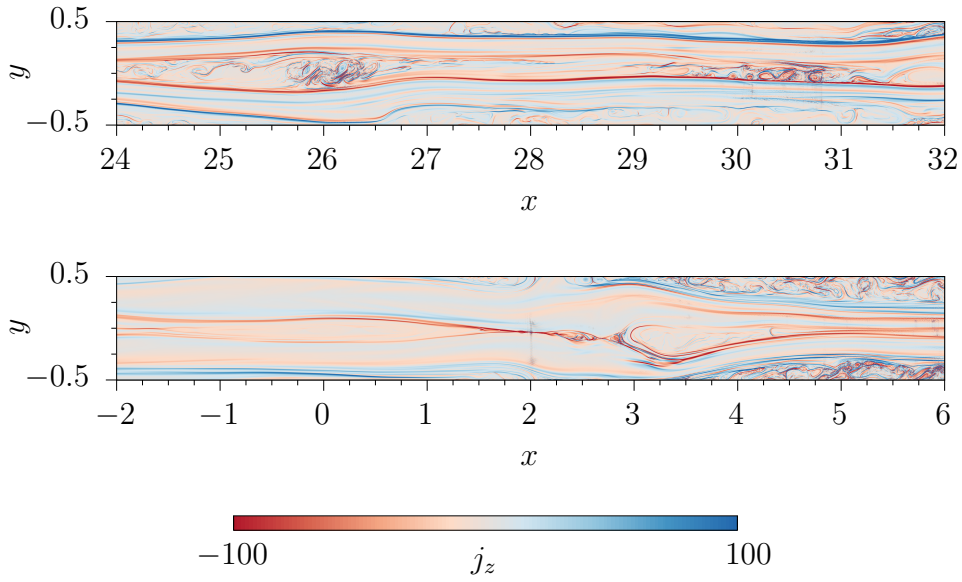

Figure 4.3: Typical contours of the current j_z for $S = 64000$. The top panel shows a section of the domain at $t = 41$, while the bottom shows one a different section at $t = 45$. The plasmoid-like structures are not common in the flow; when present they do not fully develop, due to Alfvénic shearing flows.

may serve as proof of the principle) put forward in Loureiro and Boldyrev (2017); Mallet et al. (2017a); Boldyrev and Loureiro (2017) that the tearing instability can compete with the Alfvénic evolution of very anisotropic eddies. The spectra and alignment angle do not display a power-law scaling associated with the inertial range (see Figs. 4.5 and 4.6).

Finally, in the middle panel of Fig. 4.1 we show the case $S = 16000$ where the Alfvénic and tearing times are comparable. The energy evolution is similar to that in the case of $S = 64000$, although the saturation of the growing y-components seems to start at a slightly earlier time, in accordance with the increasing importance of the tearing process. This case is especially important for our consideration. The energy spectrum of the fluctuations is shown in Fig. 4.7 for several different instances during the eddy evolution.

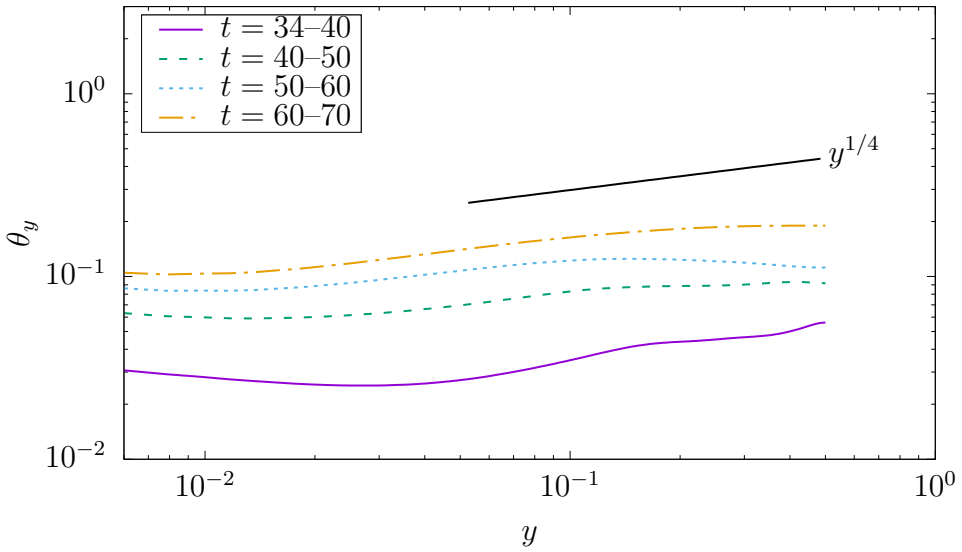

Figure 4.4: Alignment angle as a function of the short coordinate y for the setup $S = 64000$ averaged over different periods of the eddy's evolution.

We observe that as the turbulence is developing inside the eddy, its spectrum broadens in k-space and approaches a slope close to $-19/9$, consistent with the prediction for the tearing-mediated turbulence (Boldyrev and Loureiro, 2017). In this case, the tearing instability has a better chance to compete with the Alfvénic fluctuations. The more pronounced plasmoid-like current structures observed in this case—see Fig. 4.8—strengthen this interpretation. At the very late stages of the eddy evolution, when the anisotropic eddy is destroyed, the spectrum of the resulting steady-state fluctuations seems to be approaching the shallower $-3/2$ spectrum of regular MHD turbulence.

The alignment angle measured for the case of $S = 16000$ however shows a difference with the predictions of (Boldyrev and Loureiro, 2017). Fig. 4.9 shows that the alignment angle does not increase at small scales, as predicted in (Boldyrev and Loureiro, 2017). The reason for that is presently not clear. It may be related to the principal differences between the 2D and 3D cases, to the limited Reynolds number, or it may indicate that the assumption

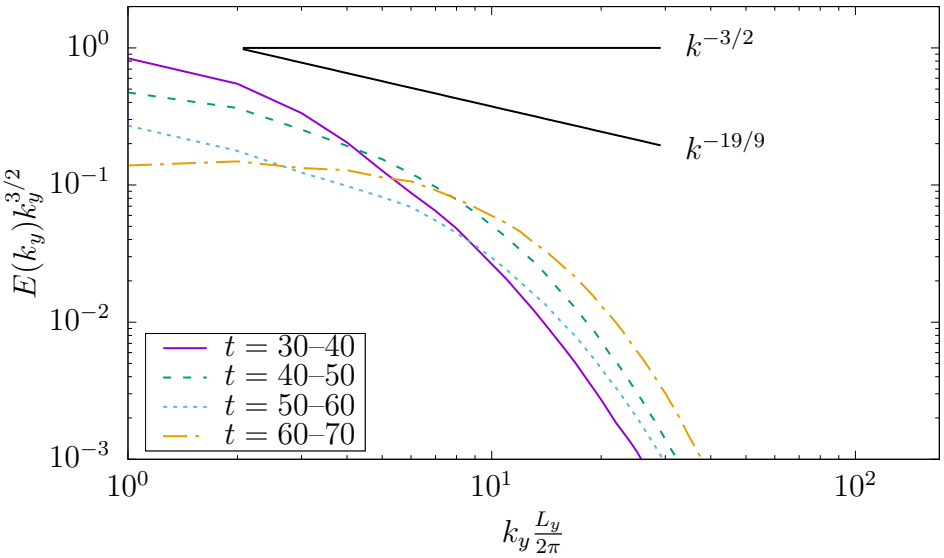

Figure 4.5: Compensated energy spectrum for setup $S = 4000$ for several intermediate moments during the eddy evolution. An inertial range power law is not observed, as this case has both a smaller Reyndolds number and is dominated by the tearing mode.

of Alfvénization of tearing-mediated turbulence made in (Boldyrev and Loureiro, 2017) is incorrect.

4.3 Conclusions

It has been proposed in (Loureiro and Boldyrev, 2017; Mallet et al., 2017a; Boldyrev and Loureiro, 2017) that tearing instability can play a significant role in the inertial interval of magnetic turbulence at small scales. Very recently, detailed analytical and observational studies of this phenomenon have been conducted (Mallet et al., 2017b; Loureiro and Boldyrev, 2017; Comisso et al., 2018; Vech et al., 2018). In this work, we have presented a numerical study of an interplay between non-linear Alfvénic interactions and tearing instabilities in MHD turbulence. Our results indicate that the

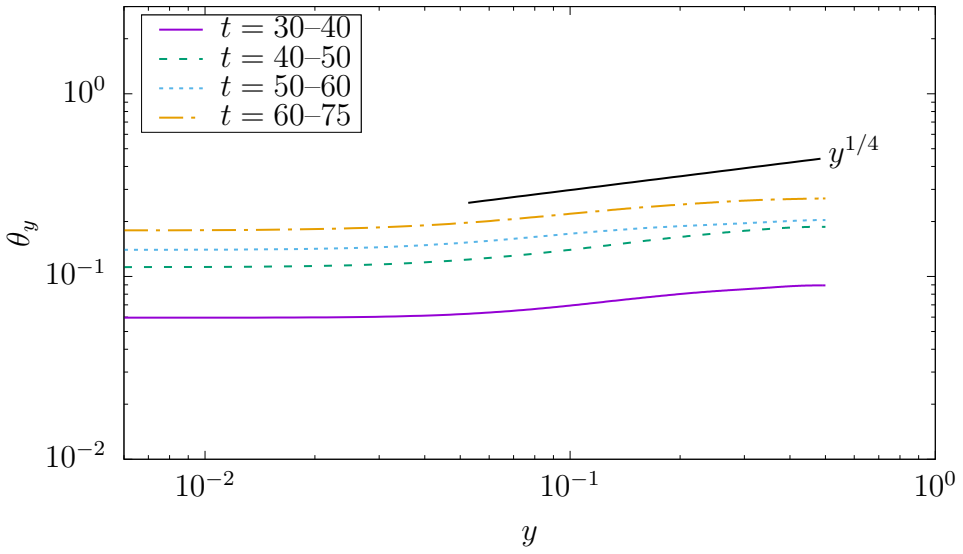

Figure 4.6: Alignment angle for setup $S = 4000$ averaged over different periods of the eddy's evolution.

tearing instability can indeed modify the dynamics of highly anisotropic turbulent eddies. In agreement with the analytic predictions, this process can lead to a new regime of MHD turbulence at scales larger than the dissipation scale.

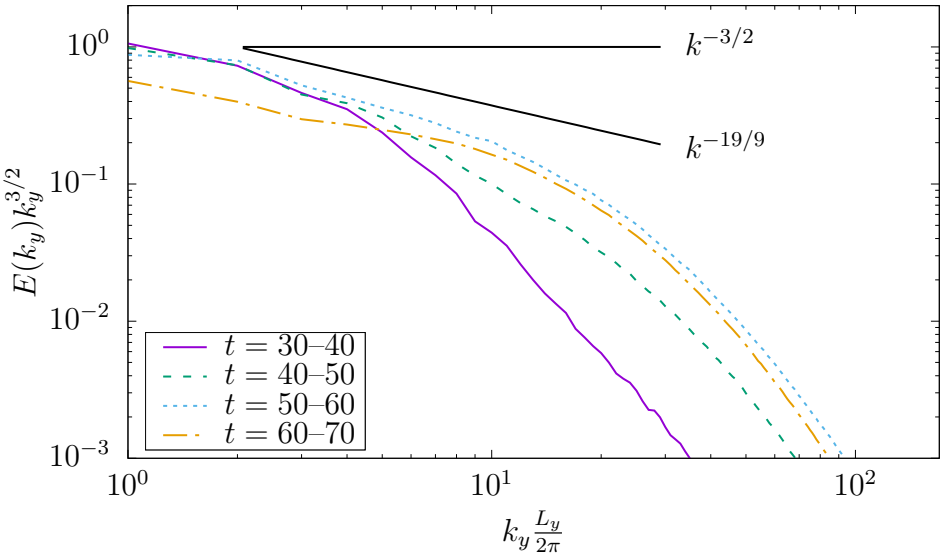

Figure 4.7: Compensated energy spectrum for setup $S = 16000$ for several intermediate moments during the eddy evolution. The spectrum broadens in k-space and seems to approach the slope of $-19/9$, consistent with the prediction for the tearing-mediated turbulence, before the eddy is destroyed at late times.

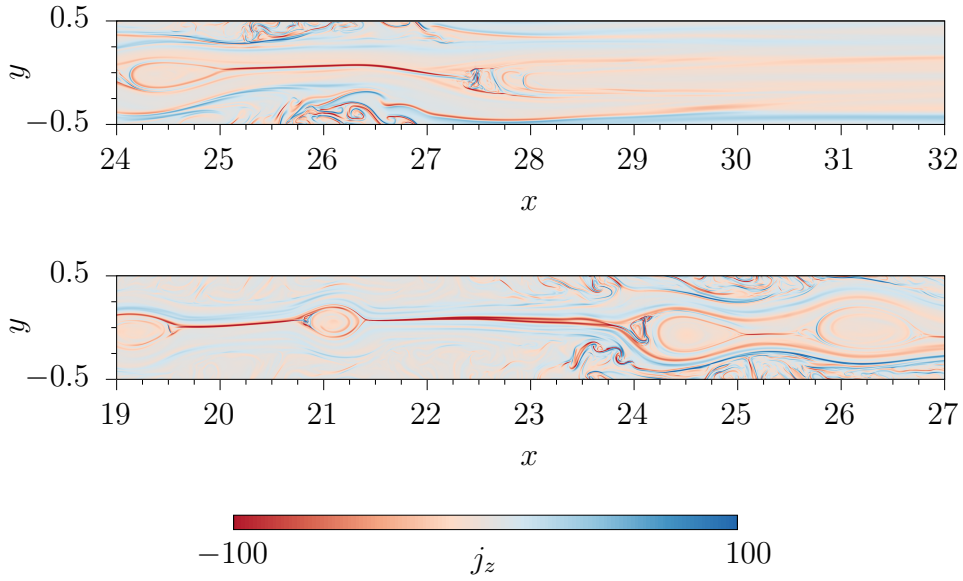

Figure 4.8: Typical contours of the current j_z for $S = 16000$. The top panel shows a section of the domain at $t = 40$, while the bottom one shows a different section at $t = 45$. The tendency of turbulence to create plasmoid-like structures is more pronounced as compared to the case depicted in Fig 4.3.

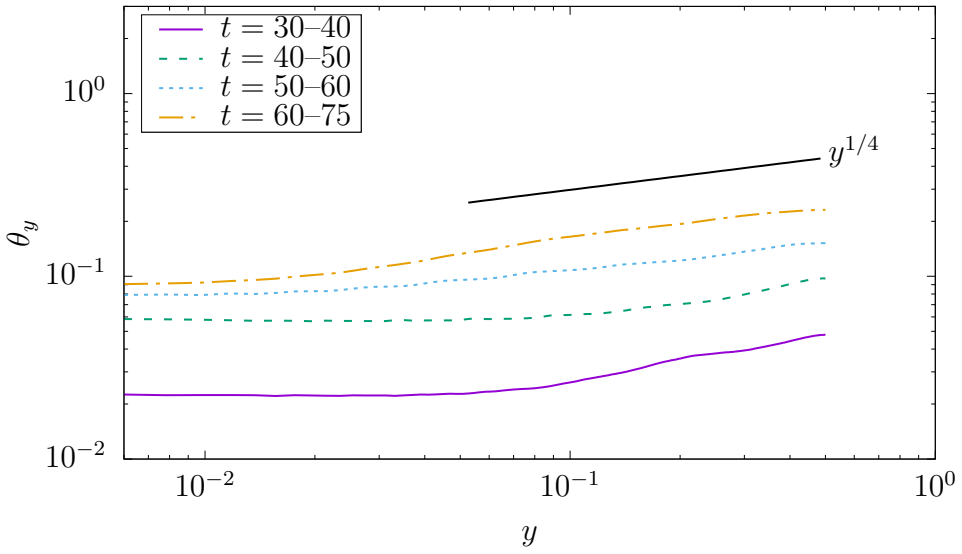

Figure 4.9: Alignment angle for setup $S = 16000$ averaged over different periods of the eddy's evolution.

5 CONCLUSION

This thesis explored the turbulence generated by magnetic instabilities in systems with a large-scale shear. Specifically, we examined the local turbulence produced as a result of the nonlinear saturation of the MRI and the effect that the tearing instability has on strongly-sheared Alfvénic eddies in the MHD cascade. By using large-scale numerical computations, we characterized the turbulence in these systems and compared results with phenomenological models. We were able to identify key features that either validate current models or provide a basis for future models.

5.1 MRI-driven turbulence with a net magnetic flux

We characterized the turbulence driven by the MRI and compared it with both computations and theory of strong, driven (externally forced) MHD turbulence. In contrast with the incompressible, resistive MHD equations in a non-rotating, non-shearing frame, the shearing-box (SB) model includes extra terms that a priori cannot be neglected in the analysis of the turbulence. Particularly, a constant, linear shear term—a consequence of differential rotation in the systems modeled by the SB equations—exists in both the momentum and induction equations and is responsible for injecting energy on a broad range of scales.

This work demonstrated that for a range of scales smaller than the system size, this shear is, in fact, a minor source of the energy. The main source of energy is the nonlinear transfer. Therefore, one can rely again on phenomological arguments of scale-by-scale energy transfer. This was validated by evidence of a power-law spectrum for the energy that was very close to $E(k) \sim k^{-3/2}$.

The shearing-box system sources energy from the shear stresses mentioned above as well as the unstable modes of the MRI. In order to determine the outer scale of the turbulence, one cannot rely on a forcing scale. We were able to identify the outer scale as that scale where the linear shear and the turbulent shear are balanced, i.e.

$$\frac{\lambda_0}{v_0} \sim r\frac{\mathrm{d}\,\Omega}{\mathrm{d}\,r}. \tag{5.1}$$

This outer scale adjusts itself with the imposed magnetic field strength such that the turbulence at scales below this outer scale is self-similar.

These results all point toward the similarity of the inertial range dynamics of the net-flux, MRI-driven shearing box with those of the DA theory, allowing the reuse of much of what was understood previously.

5.2 MRI dynamo and self-sustained turbulence

We investigated the conditions under which the dynamo effect present in the zero-net-flux shearing box is strong enough to self sustain a turbulent state with positive angular momentum transport. Unlike the case of forced MHD, it was not estabilished that a turbulent dynamo would exist for any magnetic Prandtl number as long as the Reynolds number were sufficiently high. Work that we performed indicates that what is important is that sufficiently anisotropic modes can exist and interact nonlinearly.

In numerical solutions without a net flux, we found that the transport α depends significantly on the aspect ratio of the box. For "tall" shearing boxes ($L_z > L_x$), the subcritical MRI dynamo more easily operates, and the transport is increased. We proposed that this is because by constraining the size of eddies to the radial extent of the box, turbulent mixing of the azimuthal magnetic field is prevented. This allows the system to vertically

separate large amounts of magentic flux, effectively creating smaller regions of net flux, where the MRI can operate. In the case of "short" shearing boxes ($L_z < L_x$), the eddy size is not constrained by the small radial extent. Instead, the outer scale of the turbulence—as we determined in early work—sets the relevant eddy size. We were able to support this explanation with a numerical computation of a short box that exhibited self-sustained turbulence on small scales.

5.3 Tearing mode competition with Alfvénic dynamics

In an effort to study the deep inertial range of MHD turbulence, we proposed a method for simulating the two-dimensional dynamics of a highly anisotropic eddy. Such an eddies are predicted by the DA theory, and in plasma systems with $S > 10^7$, are predicted to become unstable to the tearing mode at scales smaller than a critical scale. Our method was to produce a critically-balanced eddy at the box scale and drive turbulence at smaller scales.

An eddy in the inertial range will live for its turnover time: in this case, the Alvfén crossing time of the box. However, if the timescale of a tearing mode in this box is shorter than the eddy crossing time, the tearing mode can decorrelate the eddy on this time scale instead. By varying the resistivity of the system we were able demonstrate that such an instability can indeed compete with the turbulence of the system. As resistivity was increased, the eddy was disrupted on time scales shorter than the Alfvén time.

We were further able to establish that when the two time scales are comparable that the energy spectrum displays a power-law scaling that is close to what is predicted by recent theories of "tearing-mediated turbulence." Other characteristics of this regime were not supported, such as the reduction of alignment at smaller scales.

5.4 Future research

MRI and dynamo in the shearing box

Our work understanding the turbulunce within the shearing box suggests further work, particulary in understanding the dynamo mechanism within systems zero net-flux.

The system was found to be very sensitive to the anisotropy of the box. A natural question to answer is whether an asymptotic regime is reached with respect to this aspect ratio. That is, should the box be stretched further in a particular dimension, will the mean measure of turbulent transport α and the size of structures in the box no longer depend on the box size?

Given that the magnetic structures created by the constant shear are strong and elongated in the azimuthal direction, could the tearing instability become important in the fully nonlinear regime? Could this explain the additional difficulty in establishing the dynamo effect for $\mathrm{Pm} < 1$?

Another area that remains unexplored is the role of helicity in the dynamo process. We briefly tested the idea that adding or removing helicity from the solutions would affect whether the MRI would be able to support self-sustained turbulence through the dynamo effect, but our results were inconclusive. Boundary conditions that would allow the escape of helicity could also be used to study this effect. A more thorough investigation of this effect is warranted.

Tearing-mediated turbulence

Our work and that of Dong et al. (2018) provided evidence in two dimensions for the new tearing-mediated regime of MHD turbulence. However, the work is far from conclusive. The range of the power law is short, and its precise exponent hasn't been determined. Also, the alignment angle scaling doesn't match theory.

The clearest next steps would be to attempt another set of these two-dimensional computations with more anisotropic boxes at higher S. Another option is to use an isotropic two-dimensional setup that starts from the outer scale of turbulence—similar to the method of Dong et al. (2018). This would allow further confirmation of at least the spectral scaling.

It may be that a three-dimensional setup is required to produce all of the features of this regime. Unfortunately, the computing resources available currently are orders of magnitude less than what is needed in order to simulate this regime in three dimensions starting from the outer scale. An alternative, would be to extend our method to three dimensions. Even then, the costs are currently prohibitive.

Our work and its theoretical underpinnings point toward the intimate connection between magnetic reconnection and turbulence. Both turbulence and reconnection have been proposed as mechanisms for particle acceleration and heating. This has implications for understanding and modeling these mechanisms in plasma systems. Our setup is very similar to those of fluid models of reconnection and could be used along with particle tracking or with kinetic models to determine the dominant acceleration mechanisms.

REFERENCES

Abramowicz, Marek A., and P. Chris Fragile. 2013. Foundations of Black Hole Accretion Disk Theory. *Living Reviews in Relativity* 16(1):1.

Balbus, S. A., and J. F. Hawley. 1991. A powerful local shear instability in weakly magnetized disks. I - Linear analysis. II - Nonlinear evolution. *Astrophys. J.* 376:214–233.

———. 1992. A Powerful Local Shear Instability in Weakly Magnetized Disks. IV. Nonaxisymmetric Perturbations. *Astrophys. J.* 400:610–621.

Balbus, S. A., and P. Henri. 2008. On the Magnetic Prandtl Number Behavior of Accretion Disks. *Astrophys. J.* 674:408–414.

Biskamp, D. 2003. *Magnetohydrodynamic Turbulence*. Cambridge University Press.

Biskamp, D., and E. Schwarz. 2001. On two-dimensional magnetohydrodynamic turbulence. *Physics of Plasmas* 8:3282–3292.

Bodo, G., A. Mignone, F. Cattaneo, P. Rossi, and A. Ferrari. 2008. Aspect ratio dependence in magnetorotational instability shearing box simulations. *A&A* 487:1–5.

Boldyrev, S. 2005. On the Spectrum of Magnetohydrodynamic Turbulence. *Astrophys. J. Lett.* 626:L37–L40.

———. 2006. Spectrum of Magnetohydrodynamic Turbulence. *Physical Review Letters* 96(11):115002.

Boldyrev, S., and F. Cattaneo. 2004. Magnetic-Field Generation in Kolmogorov Turbulence. *Physical Review Letters* 92(14):144501.

Boldyrev, S., F. Cattaneo, and R. Rosner. 2005. Magnetic-Field Generation in Helical Turbulence. *Physical Review Letters* 95(25):255001.

Boldyrev, S., and N. F. Loureiro. 2017. Magnetohydrodynamic Turbulence Mediated by Reconnection. *Astrophys. J.* 844:125.

Canuto, Claudio, M Yousuff Hussaini, Alfio Quarteroni, and Thomas A Zang. 2006. Spectral methods. scientific computation. *Fundamentals in Single Domains*.

Carbone, V., P. Veltri, and A. Mangeney. 1990. Coherent structure formation and magnetic field line reconnection in magnetohydrodynamic turbulence. *Physics of Fluids A* 2:1487–1496.

Chandran, B. D. G., A. A. Schekochihin, and A. Mallet. 2015. Intermittency and Alignment in Strong RMHD Turbulence. *Astrophys. J.* 807:39.

Chandrasekhar, S. 1960. The Stability of Non-Dissipative Couette Flow in Hydromagnetics. *Proceedings of the National Academy of Science* 46: 253–257.

Chen, C. H. K. 2016. Recent progress in astrophysical plasma turbulence from solar wind observations. *Journal of Plasma Physics* 82(6):535820602.

Chen, C. H. K., and S. Boldyrev. 2017. Nature of Kinetic Scale Turbulence in the Earth's Magnetosheath. *The Astrophysical Journal* 842:122.

Chen, C. H. K., A. Mallet, T. A. Yousef, A. A. Schekochihin, and T. S. Horbury. 2011. Anisotropy of Alfvénic turbulence in the solar wind and numerical simulations. *MNRAS* 415:3219–3226.

Comisso, L., Y.-M. Huang, M. Lingam, E. Hirvijoki, and A. Bhattacharjee. 2018. Magnetohydrodynamic Turbulence in the Plasmoid-mediated Regime. *Astrophys. J.* 854:103.

Coppi, B., R. Galvao, R. Pellat, M. Rosenbluth, and P. Rutherford. 1976. Resistive internal kink modes. *Fizika Plazmy* 2:961–966.

Davidson, Peter Alan. 2017. *Introduction to magnetohydrodynamics*, vol. 25. 2nd ed. Cambridge University Press.

Dobrowolny, M., P. Veltri, and A. Mangeney. 1983. Dissipative instabilities of magnetic neutral layers with velocity shear. *Journal of Plasma Physics* 29:393–407.

Dong, Chuanfei, Liang Wang, Yi-Min Huang, Luca Comisso, and Amitava Bhattacharjee. 2018. Role of the plasmoid instability in magnetohydrodynamic turbulence. *Phys. Rev. Lett.* 121:165101.

Einaudi, G., and F. Rubini. 1986. Resistive instabilities in a flowing plasma. I - Inviscid case. *Physics of Fluids* 29:2563–2568.

Event Horizon Telescope Collaboration, Kazunori Akiyama, Antxon Alberdi, Walter Alef, Keiichi Asada, Rebecca Azulay, Anne-Kathrin Baczko, David Ball, Mislav Baloković, John Barrett, Dan Bintley, Lindy Blackburn, Wilfred Boland, Katherine L. Bouman, Geoffrey C. Bower, Michael Bremer, Christiaan D. Brinkerink, Roger Brissenden, Silke Britzen, Avery E. Broderick, Dominique Broguiere, Thomas Bronzwaer, Do-Young Byun, John E. Carlstrom, Andrew Chael, Chi-kwan Chan, Shami Chatterjee, Koushik Chatterjee, Ming-Tang Chen, Yongjun Chen, Ilje Cho, Pierre Christian, John E. Conway, James M. Cordes, Geoffrey B. Crew, Yuzhu Cui, Jordy Davelaar, Mariafelicia De Laurentis, Roger Deane, Jessica Dempsey, Gregory Desvignes, Jason Dexter, Sheperd S. Doeleman, Ralph P. Eatough, Heino Falcke, Vincent L. Fish, Ed Fomalont, Raquel Fraga-Encinas, William T. Freeman, Per Friberg, Christian M. Fromm, José L. Gómez, Peter Galison, Charles F. Gammie, Roberto García, Olivier Gentaz, Boris Georgiev, Ciriaco Goddi, Roman Gold, Minfeng Gu, Mark Gurwell, Kazuhiro Hada, Michael H. Hecht, Ronald Hesper, Luis C. Ho, Paul Ho, Mareki Honma, Chih-Wei L. Huang, Lei Huang, David H. Hughes, Shiro Ikeda, Makoto Inoue, Sara Issaoun, David J. James, Buell T. Jannuzi,

Michael Janssen, Britton Jeter, Wu Jiang, Michael D. Johnson, Svetlana Jorstad, Taehyun Jung, Mansour Karami, Ramesh Karuppusamy, Tomohisa Kawashima, Garrett K. Keating, Mark Kettenis, Jae-Young Kim, Junhan Kim, Jongsoo Kim, Motoki Kino, Jun Yi Koay, Patrick M. Koch, Shoko Koyama, Michael Kramer, Carsten Kramer, Thomas P. Krichbaum, Cheng-Yu Kuo, Tod R. Lauer, Sang-Sung Lee, Yan-Rong Li, Zhiyuan Li, Michael Lindqvist, Kuo Liu, Elisabetta Liuzzo, Wen-Ping Lo, Andrei P. Lobanov, Laurent Loinard, Colin Lonsdale, Ru-Sen Lu, Nicholas R. MacDonald, Jirong Mao, Sera Markoff, Daniel P. Marrone, Alan P. Marscher, Iván Martí-Vidal, Satoki Matsushita, Lynn D. Matthews, Lia Medeiros, Karl M. Menten, Yosuke Mizuno, Izumi Mizuno, James M. Moran, Kotaro Moriyama, Monika Moscibrodzka, Cornelia Müller, Hiroshi Nagai, Neil M. Nagar, Masanori Nakamura, Ramesh Narayan, Gopal Narayanan, Iniyan Natarajan, Roberto Neri, Chunchong Ni, Aristeidis Noutsos, Hiroki Okino, Héctor Olivares, Tomoaki Oyama, Feryal Özel, Daniel C. M. Palumbo, Nimesh Patel, Ue-Li Pen, Dominic W. Pesce, Vincent Piétu, Richard Plambeck, Aleksand ar PopStefanija, Oliver Porth, Ben Prather, Jorge A. Preciado-López, Dimitrios Psaltis, Hung-Yi Pu, Venkatessh Ramakrishnan, Ramprasad Rao, Mark G. Rawlings, Alexander W. Raymond, Luciano Rezzolla, Bart Ripperda, Freek Roelofs, Alan Rogers, Eduardo Ros, Mel Rose, Arash Roshanineshat, Helge Rottmann, Alan L. Roy, Chet Ruszczyk, Benjamin R. Ryan, Kazi L. J. Rygl, Salvador Sánchez, David Sánchez-Arguelles, Mahito Sasada, Tuomas Savolainen, F. Peter Schloerb, Karl-Friedrich Schuster, Lijing Shao, Zhiqiang Shen, Des Small, Bong Won Sohn, Jason SooHoo, Fumie Tazaki, Paul Tiede, Remo P. J. Tilanus, Michael Titus, Kenji Toma, Pablo Torne, Tyler Trent, Sascha Trippe, Shuichiro Tsuda, Ilse van Bemmel, Huib Jan van Langevelde, Daniel R. van Rossum, Jan Wagner, John Wardle, Jonathan Weintroub, Norbert Wex, Robert Wharton, Maciek Wielgus, George N. Wong, Qingwen Wu, André Young, Ken Young, Ziri Younsi, Feng Yuan, Ye-Fei Yuan, J. Anton

Zensus, Guangyao Zhao, Shan-Shan Zhao, Ziyan Zhu, Joseph R. Farah, Zheng Meyer-Zhao, Daniel Michalik, Andrew Nadolski, Hiroaki Nishioka, Nicolas Pradel, Rurik A. Primiani, Kamal Souccar, Laura Vertatschitsch, and Paul Yamaguchi. 2019. First M87 Event Horizon Telescope Results. IV. Imaging the Central Supermassive Black Hole. *Astrophys. J. Lett.* 875(1): L4.

Flanagan, K., M. Clark, C. Collins, C. M. Cooper, I. V. Khalzov, J. Wallace, and C. B. Forest. 2015. Prospects for observing the magnetorotational instability in the plasma Couette experiment. *Journal of Plasma Physics* 81(4):345810401.

Frigo, Matteo, and Steven G Johnson. 2005. The design and implementation of fftw3. *Proceedings of the IEEE* 93(2):216–231.

Frisch, U. 1995. *Turbulence: The Legacy of A.N. Kolmogorov*. Cambridge University Press.

Fromang, S. 2010. MHD simulations of the magnetorotational instability in a shearing box with zero net flux: the case Pm = 4. *A&A* 514:L5.

Fromang, S., and J. Papaloizou. 2007. MHD simulations of the magnetorotational instability in a shearing box with zero net flux. I. The issue of convergence. *A&A* 476:1113–1122.

Fromang, S., J. Papaloizou, G. Lesur, and T. Heinemann. 2007. MHD simulations of the magnetorotational instability in a shearing box with zero net flux. II. The effect of transport coefficients. *A&A* 476:1123–1132.

Furth, Harold P., John Killeen, and Marshall N. Rosenbluth. 1963. Finite-resistivity instabilities of a sheet pinch. *Physics of Fluids* 6:459–484.

Galeev, A. A., R. Rosner, and G. S. Vaiana. 1979. Structured coronae of accretion disks. *Astrophys. J.* 229:318–326.

Galtier, S., S. V. Nazarenko, A. C. Newell, and A. Pouquet. 2000. A weak turbulence theory for incompressible magnetohydrodynamics. *Journal of Plasma Physics* 63:447–488.

Gissinger, C., H. Ji, and J. Goodman. 2011. Instabilities in magnetized spherical Couette flow. *Physical Review E* 84(2):026308.

Goldreich, P., and D. Lynden-Bell. 1965. II. Spiral arms as sheared gravitational instabilities. *MNRAS* 130:125.

Goldreich, P., and S. Sridhar. 1995. Toward a theory of interstellar turbulence. 2: Strong alfvenic turbulence. *The Astrophysical Journal* 438: 763–775.

———. 1997. Magnetohydrodynamic Turbulence Revisited. *Astrophys. J.* 485:680–688.

Goodman, J., and G. Xu. 1994. Parasitic instabilities in magnetized, differentially rotating disks. *Astrophys. J.* 432:213–223.

Haugen, Nils Erland L., A. Brandenburg, and W. Dobler. 2004. Simulations of nonhelical hydromagnetic turbulence. *Physical Review E* 70(1):016308.

Hawley, J. F., C. F. Gammie, and S. A. Balbus. 1995. Local Three-dimensional Magnetohydrodynamic Simulations of Accretion Disks. *Astrophys. J.* 440:742.

Herault, J., F. Rincon, C. Cossu, G. Lesur, G. I. Ogilvie, and P.-Y. Longaretti. 2011. Periodic magnetorotational dynamo action as a prototype of nonlinear magnetic-field generation in shear flows. *Physical Review E* 84(3):036321.

Hoffman, I. 1975. I. hoffman, plasma phys. 17, 143 (1975). *Plasma Phys.* 17:143.

Hu, Di, Amitava Bhattacharjee, and Yi-Min Huang. 2018. Energy spectrum of tearing mode turbulence in sheared background field. *Physics of Plasmas* 25(6):062305.

Huang, Y.-M., and A. Bhattacharjee. 2016. Turbulent Magnetohydrodynamic Reconnection Mediated by the Plasmoid Instability. *The Astrophysical Journal* 818:20.

Iroshnikov, P. S. 1963. Turbulence of a Conducting Fluid in a Strong Magnetic Field. *Astronomicheskii Zhurnal* 40:742.

Iskakov, A. B., A. A. Schekochihin, S. C. Cowley, J. C. McWilliams, and M. R. E. Proctor. 2007. Numerical Demonstration of Fluctuation Dynamo at Low Magnetic Prandtl Numbers. *Physical Review Letters* 98(20):208501.

Ji, H., and S. Balbus. 2013. Angular momentum transport in astrophysics and in the lab. *Physics Today* 66(8):27.

Johansen, A., A. Youdin, and H. Klahr. 2009. Zonal Flows and Long-lived Axisymmetric Pressure Bumps in Magnetorotational Turbulence. *Astrophys. J.* 697:1269–1289.

Kadomtsev, B. B., and O. P. Pogutse. 1974. Nonlinear helical perturbations of a plasma in the tokamak. *Soviet Journal of Experimental and Theoretical Physics* 38:283–290.

Kagan, D., and J. C. Wheeler. 2014. The Role of the Magnetorotational Instability in the Sun. *Astrophys. J.* 787:21.

Kolmogorov, A. 1941a. The Local Structure of Turbulence in Incompressible Viscous Fluid for Very Large Reynolds' Numbers. *Akademiia Nauk SSSR Doklady* 30:301–305.

Kolmogorov, A. N. 1962. A refinement of previous hypotheses concerning the local structure of turbulence in a viscous incompressible fluid at high Reynolds number. *Journal of Fluid Mechanics* 13:82–85.

Kolmogorov, Andrey Nikolaevich. 1941b. Dissipation of Energy in Locally Isotropic Turbulence. *Akademiia Nauk SSSR Doklady* 32:16.

Kraichnan, R. H. 1965. Inertial-Range Spectrum of Hydromagnetic Turbulence. *Physics of Fluids* 8:1385–1387.

Kraichnan, R. H., and S. Nagarajan. 1967. Growth of Turbulent Magnetic Fields. *Physics of Fluids* 10:859–870.

Latter, H. N., S. Fromang, and J. Faure. 2015. Local and global aspects of the linear MRI in accretion discs. *MNRAS* 453:3257–3268.

Lesur, G., and P.-Y. Longaretti. 2007. Impact of dimensionless numbers on the efficiency of magnetorotational instability induced turbulent transport. *MNRAS* 378:1471–1480.

———. 2011. Non-linear energy transfers in accretion discs MRI turbulence. I. Net vertical field case. *A&A* 528:A17.

Lesur, G., and G. I. Ogilvie. 2008. On self-sustained dynamo cycles in accretion discs. *A&A* 488:451–461.

———. 2010. On the angular momentum transport due to vertical convection in accretion discs. *MNRAS* 404:L64–L68.

Longaretti, P.-Y., and G. Lesur. 2010. MRI-driven turbulent transport: the role of dissipation, channel modes and their parasites. *A&A* 516:A51.

Loureiro, N. F., and S. Boldyrev. 2017. Collisionless Reconnection in Magnetohydrodynamic and Kinetic Turbulence. *Astrophys. J.* 850:182.

Loureiro, N. F., A. A. Schekochihin, and S. C. Cowley. 2007. Instability of current sheets and formation of plasmoid chains. *Physics of Plasmas* 14(10):100703–100703–4.

Loureiro, Nuno F., and Stanislav Boldyrev. 2017. Role of magnetic reconnection in magnetohydrodynamic turbulence. *Physical Review Letters* 118: 245101.

Mallet, A., A. A. Schekochihin, and B. D. G. Chandran. 2017a. Disruption of Alfvénic turbulence by magnetic reconnection in a collisionless plasma. *Journal of Plasma Physics* 83(6):905830609.

———. 2017b. Disruption of sheet-like structures in Alfvénic turbulence by magnetic reconnection. *MNRAS* 468:4862–4871.

Mallet, A., A. A. Schekochihin, B. D. G. Chandran, C. H. K. Chen, T. S. Horbury, R. T. Wicks, and C. C. Greenan. 2016. Measures of three-dimensional anisotropy and intermittency in strong Alfvénic turbulence. *Monthly Notices of the Royal Astronomical Society* 459:2130–2139.

Malyshkin, L. M., and S. Boldyrev. 2010. Magnetic Dynamo action at Low Magnetic Prandtl Numbers. *Physical Review Letters* 105(21):215002.

Maron, J., and P. Goldreich. 2001. Simulations of Incompressible Magnetohydrodynamic Turbulence. *Astrophys. J.* 554:1175–1196.

Mason, J., F. Cattaneo, and S. Boldyrev. 2008. Numerical measurements of the spectrum in magnetohydrodynamic turbulence. *Physical Review E* 77(3):036403.

Mason, J., J. C. Perez, S. Boldyrev, and F. Cattaneo. 2012. Numerical simulations of strong incompressible magnetohydrodynamic turbulence. *Physics of Plasmas* 19(5):055902.

Mason, Joanne, Fausto Cattaneo, and Stanislav Boldyrev. 2006. Dynamic Alignment in Driven Magnetohydrodynamic Turbulence. *Physical Review Letters* 97(25):255002.

Meheut, H., S. Fromang, G. Lesur, M. Joos, and P.-Y. Longaretti. 2015. Angular momentum transport and large eddy simulations in magnetorotational turbulence: the small Pm limit. *A&A* 579:A117.

Mininni, P. D., and A. Pouquet. 2007. Energy Spectra Stemming from Interactions of Alfvén Waves and Turbulent Eddies. *Physical Review Letters* 99(25):254502.

Montgomery, David, and William H. Matthaeus. 1995. Anisotropic Modal Energy Transfer in Interstellar Turbulence. *Astrophys. J.* 447:706.

Müller, W. C., and R. Grappin. 2005. Spectral Energy Dynamics in Magnetohydrodynamic Turbulence. *Physical Review Letters* 95(11):114502.

Nauman, Farrukh, and Martin E. Pessah. 2016. Sustained turbulence in differentially rotating magnetized fluids at low magnetic prandtl number. *The Astrophysical Journal* 833(2):187.

Ng, C. S., and A. Bhattacharjee. 1996. Interaction of Shear-Alfven Wave Packets: Implication for Weak Magnetohydrodynamic Turbulence in Astrophysical Plasmas. *Astrophys. J.* 465:845.

———. 2007. Anisotropic MHD turbulence. In *Turbulence and nonlinear processes in astrophysical plasmas*, ed. D. Shaikh and G. P. Zank, vol. 932 of *American Institute of Physics Conference Series*, 137–143.

Oughton, S., W. H. Matthaeus, and P. Dmitruk. 2017. Reduced MHD in Astrophysical Applications: Two-dimensional or Three-dimensional? *Astrophys. J.* 839:2.

Perez, J. C., and S. Boldyrev. 2010a. Strong magnetohydrodynamic turbulence with cross helicity. *Physics of Plasmas* 17(5):055903.

———. 2010b. Strong magnetohydrodynamic turbulence with cross helicity. *Physics of Plasmas* 17(5):055903.

Perez, J. C., J. Mason, S. Boldyrev, and F. Cattaneo. 2014a. Comment on the numerical measurements of the magnetohydrodynamic turbulence spectrum by A. Beresnyak (Phys. Rev. Lett. 106 (2011) 075001; MNRAS 422 (2012) 3495; ApJ 784 (2014) L20). *ArXiv e-prints*.

———. 2014b. Scaling Properties of Small-scale Fluctuations in Magnetohydrodynamic Turbulence. *Astrophys. J. Lett.* 793:L13.

Perez, Jean Carlos, Joanne Mason, Stanislav Boldyrev, and Fausto Cattaneo. 2012. On the energy spectrum of strong magnetohydrodynamic turbulence. *Phys. Rev. X* 2(4):041005.

Pessah, M. E., and C.-k. Chan. 2008. Viscous, Resistive Magnetorotational Modes. *Astrophys. J.* 684:498–514.

Petitdemange, L., E. Dormy, and S. A. Balbus. 2008. Magnetostrophic MRI in the Earth's outer core. *Geophys. Res. Lett.* 35:15305.

Politano, H., A. Pouquet, and V. Carbone. 1998. Determination of anomalous exponents of structure functions in two-dimensional magnetohydrodynamic turbulence. *EPL (Europhysics Letters)* 43:516–521.

Rempel, Erico L., Geoffroy Lesur, and Michael R. E. Proctor. 2010. Supertransient magnetohydrodynamic turbulence in keplerian shear flows. *Phys. Rev. Lett.* 105:044501.

Richardson, Lewis Fry. 1922. *Weather prediction by numerical process*. Cambridge University Press.

———. 2007. *Weather prediction by numerical process*. Cambridge University Press.

Rincon, F., G. I. Ogilvie, and M. R. E. Proctor. 2007. Self-Sustaining Nonlinear Dynamo Process in Keplerian Shear Flows. *Physical Review Letters* 98(25):254502.

Riols, A., F. Rincon, C. Cossu, G. Lesur, P.-Y. Longaretti, G. I. Ogilvie, and J. Herault. 2013. Global bifurcations to subcritical magnetorotational dynamo action in Keplerian shear flow. *Journal of Fluid Mechanics* 731: 1–45.

Riols, A., F. Rincon, C. Cossu, G. Lesur, G. I. Ogilvie, and P. Longaretti. 2016. Magnetorotational dynamo chimeras. The missing link to turbulent accretion disk dynamo models? *ArXiv e-prints*.

Riols, A., F. Rincon, C. Cossu, G. Lesur, G. I. Ogilvie, and P.-Y. Longaretti. 2015. Dissipative effects on the sustainment of a magnetorotational dynamo in Keplerian shear flow. *A&A* 575:A14.

Schekochihin, A. A., S. C. Cowley, W. Dorland, G. W. Hammett, G. G. Howes, E. Quataert, and T. Tatsuno. 2009. Astrophysical Gyrokinetics: Kinetic and Fluid Turbulent Cascades in Magnetized Weakly Collisional Plasmas. *The Astrophysical Journal Supplement* 182:310–377.

Seilmayer, M., V. Galindo, G. Gerbeth, T. Gundrum, F. Stefani, M. Gellert, G. Rüdiger, M. Schultz, and R. Hollerbach. 2014. Experimental Evidence for Nonaxisymmetric Magnetorotational Instability in a Rotating Liquid Metal Exposed to an Azimuthal Magnetic Field. *Physical Review Letters* 113(2):024505.

Shakura, N. I., and R. A. Sunyaev. 1973. Black holes in binary systems. Observational appearance. *A&A* 24:337–355.

Shi, Ji-Ming, James M Stone, and Chelsea X Huang. 2016. Saturation of the magnetorotational instability in the unstratified shearing box with zero net flux: convergence in taller boxes. *Monthly Notices of the Royal Astronomical Society* 456(3):2273–2289.

Sisan, D. R., N. Mujica, W. A. Tillotson, Y.-M. Huang, W. Dorland, A. B. Hassam, T. M. Antonsen, and D. P. Lathrop. 2004. Experimental Observation and Characterization of the Magnetorotational Instability. *Physical Review Letters* 93(11):114502.

Spitzer, Lyman. 1962. *Physics of Fully Ionized Gases*. Interscience.

———. 2006. *Physics of fully ionized gases*. Courier Corporation.

Squire, J., and A. Bhattacharjee. 2014. Nonmodal Growth of the Magnetorotational Instability. *Physical Review Letters* 113(2):025006.

Sridhar, S., and P. Goldreich. 1994. Toward a Theory of Interstellar Turbulence. I. Weak Alfvenic Turbulence. *Astrophys. J.* 432:612.

Strauss, H. R. 1976. Nonlinear, three-dimensional magnetohydrodynamics of noncircular tokamaks. *Physics of Fluids* 19:134–140.

Tobias, S. M., F. Cattaneo, and S. Boldyrev. 2013. MHD Dynamos and Turbulence. In *Ten Chapters in Turbulence*, ed. P.A. Davidson, Y. Kaneda, and K.R. Sreenivasan, 351–404. Cambridge University Press.

Umurhan, O. M., and O. Regev. 2004. Hydrodynamic stability of rotationally supported flows: Linear and nonlinear 2D shearing box results. *A&A* 427:855–872.

Vainshtein, S. I., and L. L. Kichatinov. 1986. The dynamics of magnetic fields in a highly conducting turbulent medium and the generalized Kolmogorov-Fokker-Planck equations. *Journal of Fluid Mechanics* 168: 73–87.

Vech, D., A. Mallet, K. G. Klein, and J. C. Kasper. 2018. Magnetic Reconnection May Control the Ion-scale Spectral Break of Solar Wind Turbulence. *Astrophys. J. Lett.* 855:L27.

Velikhov, E. P. 1959. . *Sov. Phys. JETP* 36:1398.

Walker, J., G. Lesur, and S. Boldyrev. 2016. On the nature of magnetic turbulence in rotating, shearing flows. *MNRAS* 457:L39–L43.

Walker, Justin, and Stanislav Boldyrev. 2017. Magnetorotational dynamo action in the shearing box. *Monthly Notices of the Royal Astronomical Society* 470(3):2653–2658.

Walker, Justin, Stanislav Boldyrev, and Nuno F. Loureiro. 2018. Influence of tearing instability on magnetohydrodynamic turbulence. *Phys. Rev. E* 98:033209.

Wan, M., W. H. Matthaeus, S. Servidio, and S. Oughton. 2013. Generation of X-points and secondary islands in 2D magnetohydrodynamic turbulence. *Physics of Plasmas* 20(4):042307.

Zhdankin, V., S. Boldyrev, and J. Mason. 2017. Influence of a large-scale field on energy dissipation in magnetohydrodynamic turbulence. *MNRAS* 468:4025–4029.

Zhdankin, V., S. Boldyrev, J. C. Perez, and S. M. Tobias. 2014. Energy Dissipation in Magnetohydrodynamic Turbulence: Coherent Structures or "Nanoflares"? *Astrophys. J.* 795:127.

Zhdankin, V., D. A. Uzdensky, J. C. Perez, and S. Boldyrev. 2013. Statistical Analysis of Current Sheets in Three-dimensional Magnetohydrodynamic Turbulence. *Astrophys. J.* 771:124.